A Comparison of Convective Storm Inflow Moisture Variability between the Great Plains and the Southeastern United States Using Multiplatform Field Campaign Observations

GUO LIN,[a,b] ZHIEN WANG,[a,b] CONRAD ZIEGLER,[c,d] XIAO-MING HU,[d,e] MING XUE,[d,e] BART GEERTS,[f] AND YUFEI CHU[a,b]

[a] *Department of Atmospheric and Oceanic Sciences, University of Colorado Boulder, Boulder, Colorado*
[b] *Laboratory for Atmospheric and Space Physics, University of Colorado Boulder, Boulder, Colorado*
[c] *NOAA/National Severe Storms Laboratory, Norman, Oklahoma*
[d] *School of Meteorology, University of Oklahoma, Norman, Oklahoma*
[e] *Center for Analysis and Prediction of Storms, University of Oklahoma, Norman, Oklahoma*
[f] *Department of Atmospheric Science, University of Wyoming, Laramie, Wyoming*

(Manuscript received 5 April 2022, in final form 17 February 2023, accepted 21 February 2023)

ABSTRACT: The magnitude of water vapor content within the near-storm inflow can either support or deter the storm's upscale growth and maintenance. However, the heterogeneity of the moisture field near storms remains poorly understood because the operational observation network lacks detail. This observational study illustrates that near-storm inflow water vapor environments are both significantly heterogeneous and different than the far-inflow storm environment. This study also depicts the importance of temporal variation of water vapor mixing ratio (WVMR) to instability during the peak tornadic seasons in the U.S. Southeast and Great Plains regions during the Verification of the Origins of Rotation in Tornadoes Experiment Southeast 2018 (VSE18) campaign and the Targeted Observation by Radar and UAS of Supercells (TORUS) campaign, respectively. VSE18 results suggest that the surface processes control WVMR variation significantly in lower levels, with the highest WVMR mainly located near the surface in inflows in the southeast region. In contrast, TORUS results show more vertically homogeneous WVMR profiles and rather uniform water vapor distribution variation occurring in deep, moist stratified inflows in the Great Plains region. Temporal water vapor variations within 5-min periods could lead to over 1000 J kg^{-1} CAPE changes in both VSE18 and TORUS, which represent significant potential buoyancy perturbations for storms to intensify or decay. These temporal water vapor and instability evolutions of moving storms remain difficult to capture via radiosondes and fixed in situ or profiling instrumentation, yet may exert a strong impact on storm evolution. This study suggests that improving observations of the variability of near-storm inflow moisture can accurately refine a potential severe weather threat.

SIGNIFICANCE STATEMENT: It has long been recognized that better observations of the planetary boundary layer (PBL) inflow near convective storms are needed to improve severe weather forecasting. The current operational networks essentially do not provide profile measurements of the PBL, except for the sparsely spaced 12-hourly sounding network. More frequent geostationary satellite observations do not provide adequately high vertical resolution in the PBL. This study uses airborne lidar profiler measurements to examine moisture in the inflow region of convective storms in the Great Plains and the southeastern United States during their respective tornadic seasons. Rapid PBL water vapor variations on a ~5 min time scale can lead to CAPE perturbations exceeding 1000 J kg^{-1}, representing significant perturbations that could promote storm intensification or decay. Severe thunderstorms may generate high-impact weather phenomena, such as tornadoes, high winds, hail, and heavy rainfall, which have substantial socioeconomic impacts. Ultimately, by contrasting characteristics of the convective storm inflow in the two regions, this study may lead to a more accurate assessment of severe weather threats.

KEYWORDS: Boundary layer; Storm environments; Aircraft observations; Lidars/Lidar observations; Remote sensing

1. Introduction

Pockets of higher humidity within the low-level inflow, in combination with dynamic processes, may create conditions favorable for the formation and evolution of convective storms by lowering the lifting condensation level (LCL) and increasing the convective available potential energy (CAPE; related to the theoretical maximum updraft speed). Such moisture anomalies may contribute to the development of severe and hazardous weather events including tornadoes and flash flooding (e.g., Sherburn and Parker 2014; Nielsen et al. 2015; Geerts et al. 2017; Terti et al. 2017; Weckwerth et al. 2019). Numerous studies have pointed out the importance of the moisture field for convection formation and precipitation. For example, Crook (1996) and Weckwerth (2000) explored low-level moisture sensitivity experiments and found that even small moisture anomalies (e.g., 1 g kg^{-1}) may lead to the difference between no convection initiation and intense deep convective storms. Schumacher and Peters (2017) found that increasing water vapor mixing ratio (WVMR) by 2 g kg^{-1} in the lowest 1 km could lead to a 60% storm precipitation

Corresponding author: Zhien Wang, zhien.wang@colorado.edu

DOI: 10.1175/JTECH-D-22-0037.1

© 2023 American Meteorological Society. For information regarding reuse of this content and general copyright information, consult the AMS Copyright Policy (www.ametsoc.org/PUBSReuseLicenses).

Brought to you by NOAA Central Library | Unauthenticated | Downloaded 09/08/23 02:59 PM UTC

increase with model simulations. Moreover, the clear-air region is responsible for moisture variations that can be quite large (e.g., Weckwerth et al. 1996). A numerical sensitivity study by Schumacher (2015) showed that a decrease of column-integrated water vapor by only 0.3%–1% can reduce area-integrated precipitation maxima up to 29%. Such high sensitivity of storm behavior to the low-level near-storm moisture indicates that small moisture errors in numerical weather prediction models can lead to large errors in forecasts of convective storms and precipitation.

Water vapor near storms can change rapidly in amount and distribution due to storm-environment interactions and local surface processes. Apart from the natural evolution of the planetary boundary layer [PBL; or hereafter simply boundary layer (BL)] near a convective storm, a moving and evolving storm often substantially modifies its low-level environment immediately around the storm. Lin et al. (2019) revealed fast-changing moisture outflow boundary structures within 3 h caused by frontal and convective processes using airborne Raman lidar profiling system. Potvin et al. (2010) investigated ~1200 proximity soundings and found that soundings collected very close to storms tend to have larger variability compared to far-storm environment, due to convective feedback processes (e.g., anvil shadow, cold outflow, and precipitation). The PBL structure adjacent to a storm can differ significantly from the unperturbed PBL far from the storm (e.g., Markowski et al. 2012). Mesoscale variations in land surface type and soil moisture may result in environmental heterogeneity in the PBL that can create horizontal wind shear and convergence patterns that in turn may affect storm evolution (Katona et al. 2016).

Operational networks are unable to measure the fine-scale water vapor variations in convective storm inflows (e.g., Weckwerth 2000; Schultz and Askelson 2012; Coniglio et al. 2013; Wade et al. 2018). The fast-changing moisture in near-storm inflow could rapidly destabilize the environment to support storm development (e.g., Peters et al. 2017). The operational sounding network with a spatial density of 100 km and at a temporal frequency of once per 12 h lacks the spatiotemporal resolution to characterize the fine-scale evolution of a near-storm inflow environment, particularly water-vapor variability. Sounding-derived parameters from the near-storm environment during intensive observation periods (IOPs) of various field projects have long been used to predict various attributes of storm inflow (e.g., Maddox 1976; Kerr and Darkow 1996; Rasmussen and Blanchard 1998; Thompson et al. 2003; Davies 2004; Potvin et al. 2010), as exemplified by the mobile vehicles providing sounding and surface measurements of the near-storm environment in the International H_2O Project (IHOP_2002; Weckwerth et al. 2004) and the Plains Elevated Convection at Night (PECAN) campaign (Geerts et al. 2017). In a recent comprehensive study of nearly 1000 supercell near- and far-environmental mobile research soundings spanning three decades and 13 field projects, Coniglio and Parker (2020) presented evidence that near-environmental low-level storm inflow wind profiles differ from far storm environments. However, even research soundings during IOPs are often far removed (>10 km) from the target storm inflow. Additionally, coarse temporal resolution further limits the ability to infer the fine-scale evolution of the water vapor field in convective storm inflows. For example, Nelson et al. (2020) show via spatiotemporal autocorrelation of radiosonde data that PBL thermodynamic and kinematic fields become statistically uncorrelated on scales of 1–2 h and 30 km. Although radar-based 3D thermal–microphysical retrievals are capable of obtaining Lagrangian LCL and retrieved cloud-base heights that are consistent with lifted-parcel sounding and ceilometer estimates of cloud-base height (Buban et al. 2007; Ziegler et al. 2007; Ziegler 2013), significant overestimates of cloud-base height may persist via soundings compared with other measurements from cloud photogrammetric techniques and radars (Weckwerth et al. 1996; Weckwerth 2000). Geostationary satellites have high temporal resolution but do not provide adequate horizontal or vertical resolutions of the PBL (Kahn et al. 2011; Yang et al. 2013; Steinke et al. 2015). Due to the complex interactions of storms with their near-inflow environments, the rapidly varying near-storm environments are difficult to document via conventional observation networks.

Simulations have shown large errors in low-level moisture fields relative to observations (Peters et al. 2017; Hu et al. 2019; Carroll et al. 2021), and accurate observations of water vapor distribution in inflow are needed to improve model simulations and predictions (e.g., Crook 1996; Schumacher 2015; Schumacher and Peters 2017; Carroll et al. 2021). For instance, a mesoscale model simulation with assimilated water vapor profiles from an airborne differential absorption lidar (DIAL) showed a significant improvement in quantitative precipitation forecasting skill (e.g., Wulfmeyer et al. 2006). However, Carroll et al. (2021) found a root-mean-square error (RMSE) of 1.14 g kg^{-1} water vapor mixing ratio between airborne lidar and the Rapid Refresh analysis model in the inflow on the Great Plains, but the random errors could be significantly higher than the RMSE. Many uncertainties stem from the lack of understanding of the underlying physical processes governing storm inflow water vapor distribution, leading to poor representation within numerical models. Recent projects such as the Second Verification of the Origins of Rotation in Tornadoes Experiment (VORTEX-2; Wurman et al. 2012), the Mesoscale Predictability Experiment (MPEX; Weisman et al. 2015), PECAN (Geerts et al. 2017), the Verification of the Origins of Rotations in Tornadoes Experiment-Southeast (VORTEX-SE; Rasmussen 2015; https://www.nssl.noaa.gov/projects/vortexse/), and the Targeted Observation by Radars and UAS of Supercells (TORUS; https://www.eol.ucar.edu/field_projects/torus) have aimed at better understanding key physical processes of convective storms and the storm environment, in order to improve accuracy and reduce uncertainties in forecasting weather hazards.

Assimilation of additional and higher-resolution moisture and temperature observations holds the promise of substantially improving numerical forecasts of development and subsequent evolution of deep convection (Wulfmeyer et al. 2006; Degelia et al. 2019; Lin et al. 2021). For example, Degelia et al. (2019) and Coniglio et al. (2019) found that low-level thermodynamic profiles (water vapor and temperature) assimilated in operational forecast models could improve short-term (~6 h) forecasts of convection initiation in Great Plains. King et al. (2017) found CAPE to rapidly increase over the 3 h prior to

Brought to you by NOAA Central Library | Unauthenticated | Downloaded 09/08/23 02:59 PM UTC

the initiation of high-shear, low-CAPE (HSLC) storms in the southeastern United States. Brown et al. (2021) demonstrated that this destabilization plays a unique role in the persistence of near-sunset HSLC storms. This rapid destabilization is due to changes in low-level moisture content and is likely associated with advection in a low-level jet (LLJ) (King et al. 2017; Brown et al. 2021). Detailed observational analyses with high spatial and temporal resolution using novel profiling systems are also necessary to further our understanding of MCS–environment interactions and severe storm prediction (Weckwerth and Parsons 2006).

This paper documents the evolving vertical moisture structures in convective storm inflows, using airborne Raman lidar transects. It provides a unique thermodynamic perspective of the convective storm inflow. The primary objective of this study is to examine systematic differences in convective storm inflow between the U.S. Great Plains and Southeast regions during their respective tornadic seasons. The climatological maximum in tornadoes is in the March–June transition season across the Great Plains and the southern United States (Brooks et al. 2003; Ashley 2007; Grams et al. 2012). The southeastern United States commonly experiences devastating tornadoes under conditions that differ considerably from those typical of the Great Plains, where tornado research efforts have historically focused (Ashley 2007). Existing knowledge of supercell dynamics builds on observations in typical high-shear, and moderate- to high-CAPE environments (HSHC), which are by far the most common type of tornadic environment in the Great Plains (Rasmussen et al. 1994; Wurman et al. 2012). Severe thunderstorms have a lower probability of detection and a high false alarm ratio in environments characterized by substantial vertical wind shear and limited instability (HSLC environments), particularly during the cool season and overnight in the Southeast, relative to severe storms forming in HSHC environments in the Great Plains (Davies and Fischer 2009; Guyer and Dean 2010; Sherburn and Parker 2014; Sherburn et al. 2016; Anderson-Frey et al. 2019). The HSLC environments are less well studied and understood than the HSHC environments more typical of Great Plains tornadic storms (Thompson et al. 2004). HSLC environments are more common in the Southeast (Schneider et al. 2006; Sherburn and Parker 2014) and the nocturnal prevalence of HSLC storms in the region poses its own unique risk to the public (e.g., Ashley et al. 2008). The complex land surface conditions and terrain in the Southeast likely lead to differences in surface-layer turbulence and in PBL circulations (Kalthoff et al. 1998; Katona et al. 2016; Hu et al. 2017; Lehner and Rotach 2018). It is therefore of great importance to accurately observe PBL processes and understand their impact on the intensification of convective storms.

We also aim to better understand moisture variability in storm inflow and its impact on CAPE, by examining the subhour temporal evolution of moisture in convective storm inflows. Ultimately, by contrasting characteristics of the convective storm inflow in the two regions, this study may lead to a more accurate assessment of severe weather threat. Section 2 introduces the two field campaigns and reviews the data collection methods, the datasets, and instruments in the study. The systematic moist inflow structures in the Great Plains and Southeast regions are detailed in section 3. The temporal water vapor variations and instability are analyzed in section 4, while conclusions are presented in section 5.

2. Observations and data

a. *Airborne platform, measurement capacity, and sampling strategy*

The airborne measurements presented here have sufficient resolution to characterize the spatiotemporal heterogeneity of moisture in convective storm inflows. NOAA's Aircraft Operations Center (AOC) operates two instrumented WP-3D (P-3) Orion "Hurricane Hunter" heavy research aircraft with a track record of long-duration day–night operations in the proximity of supercell storms (Dowell et al. 1997; Ziegler et al. 2001; Jorgensen et al. 2017; Ziegler et al. 2018), in mesoscale convective systems (MCSs; Jorgensen et al. 1997; Stechman et al. 2020), in hurricanes (Rogers et al. 2012), and in dryline environments (e.g., Ziegler and Hane 1993; Ziegler and Rasmussen 1998). To supplement the observational needs for understanding deep, moist convective storm inflow processes in the Great Plains and Southeast regions, one of the P-3 aircraft (tail number N42RF) was deployed successfully to sample the inflows and internal structures of fast-moving convective storms during VSE18 and TORUS. The P-3 observations offer a unique dataset to study both inflows and storms in the two campaigns.

The University of Colorado compact Raman lidar (CRL) was deployed on the P-3 during both VSE18 and TORUS. The CRL is most sensitive at night (Mueller et al. 2017; Lin et al. 2021) or under low solar background (e.g., with optically thick clouds overhead). When the sun angle is high, the CRL (whose laser is relatively low power at 50 mJ) can still provide reliable data over a limited range (up to 1.5 km; the range of mean value could be longer) (Bergmaier et al. 2014; Liu et al. 2014). The CRL performed well on the P-3 during the VSE18 and TORUS campaigns, although CRL measurements for the first four VSE18 flights (in March 2018) were degraded by contamination of the optical window by a thin oil film during flight. This compromised water vapor estimates near the surface when the P-3 flew higher than 1.5 km (AGL; hereafter, all heights are above ground level unless explicitly noted), but the typical flight levels were around 1 km during VSE18. The quality control procedure includes masking data points at and around gates with large attenuations of Raman lidar signals by liquid clouds and WVMR estimates larger than 25 g kg^{-1} (impacted by surface). The CRL provides accurate retrievals of WVMR with a mean difference of 0.2 g kg^{-1} compared to in situ measurements in the lower troposphere at a resolution of ~300 m horizontally and ~100 m vertically (Liu et al. 2014; Wu et al. 2016; Wang 2020). In this study, the horizontal WVMR of CRL is smoothed to 1200 m by a 3 s averaging window, and the vertical resolution is 30 m. By flying repeated, reverse-course straight legs in convective storm inflow regions and following storm motion, the P-3 sampled the BL inflows with the downward-pointing CRL at high spatial and temporal resolutions to characterize the inflow heterogeneity

Brought to you by NOAA Central Library | Unauthenticated | Downloaded 09/08/23 02:59 PM UTC

and evolution. These CRL-sampled thermodynamic profiles could help improve the understanding of the characteristics of rapidly evolving low-level storm inflows.

b. *VORTEX SE 2018 overview*

The Verification of the Origins of Rotation in Tornadoes Experiment Southeast 2018 (VORTEX-SE 2018 or "VSE18") is the third year of the VORTEX-SE research program to characterize environmental factors unique to the southeastern United States (Southeast or SE for short, as denoted by the large purple box shown in Fig. 1; the domain is the region that NOAA P-3 flew during the campaign). The VORTEX-SE program seeks improved understanding relating to how these factors influence the formation, intensity, structure, and path of tornadic storms in this Southeast region (https://www.eol.ucar.edu/field_projects/vortex-se). The VORTEX-SE research program was conceived and implemented to provide the greatest possible public benefit, while simultaneously making any future tornado research programs in the Southeast more effective (Rasmussen 2015).

The Southeast commonly experiences devastating tornadoes under conditions that differ considerably from the Great Plains, where tornado research has historically focused. Ashley (2007) found that most tornado fatalities occurred in the lower–Arkansas, Tennessee, and lower–Mississippi River valleys of the southeastern United States (Ashley 2007), a region outside of traditional "tornado alley." Traditional ground-based mobile-observation field experimental strategies for sampling tornadic storms cannot be easily implemented in the SE due to complex terrain and land surface types, such as hills, trees, and harder-to-navigate roads. Moreover, the fast movement speeds of Southeast storms make them both challenging and dangerous to track and sample. Markowski and Dotzek (2011) and Satrio et al. (2020) provide evidence that there is limited understanding of the processes by which low complex terrain may create local environments favorable for tornadic storms. It is especially challenging to observe and predict non-classical severe storms in the SE using ground-based observing platforms. Airborne observations of convective storms and inflows over complex terrain are therefore critically helpful in documenting the tornadic storms, environments, and storm-environment interactions over complex terrain. The main observing platforms in VSE18 include the NOAA P-3 manned aircraft flying just outside of the storm during VSE18 carried dual tail Doppler radar (TDR), the downward-pointing CRL, and a suite of in situ state measurements at flight level (Ziegler 2019) provide unique datasets sampling convective storms and their inflows.

c. *TORUS project overview*

The TORUS (https://www.eol.ucar.edu/field_projects/torus) project deployed a broad suite of cutting-edge instrumentation in a region of ~950 000 km^2 in the Great Plains stretching from North Dakota to Texas and Iowa to Wyoming and Colorado from 13 May through 16 June 2019. A goal of the project is to describe the evolving vertical structure of the inflow region in severe thunderstorms in the Great Plains and the Southeast. Work of this type may ultimately improve forecasting for tornadoes and supercell thunderstorms (i.e., typically the parent storms of the most destructive tornadoes). The focus is on fine-scale structures undetectable by operational observational networks. The TORUS project could improve supercell and tornado forecasts by revealing the composition of severe storms undetectable by operational observational networks and relating it to known characteristics of the regularly observed larger-scale environment. The same P-3 instrumentation suite used in VSE18 was employed in TORUS (i.e., the large red box shown in Fig. 1; the domain is the area that NOAA P-3 covered during TORUS).

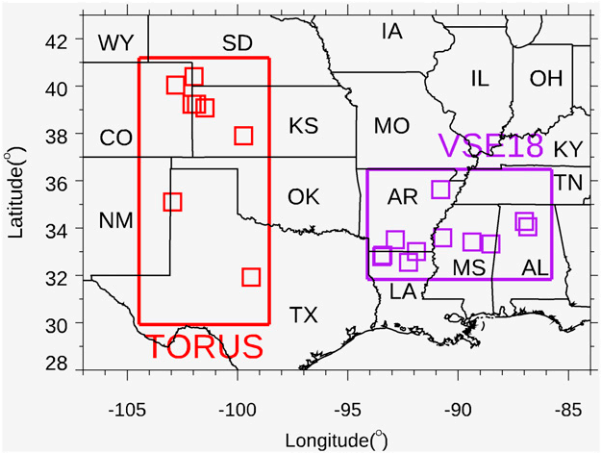

FIG. 1. The VSE18 domain (large purple box) with NOAA P-3 flight locations (small purple boxes) in the southeastern United States and the TORUS domain (large red box) with NOAA P-3 flight locations (small red boxes) in the Great Plains.

d. *NEXRAD radar*

The present study employs the operational network of Weather Surveillance Radar-1988 Doppler (WSR-88D) observations to simplify the depiction of both the targeted storms and any neighboring storms in the same larger-mesoscale region.[1] Also known as the Next Generation Weather Radar (NEXRAD) system, the WSR-88D is the second-generation operational meteorological radar of the U.S. National Weather Service (NWS). The NEXRAD radars cover a more extensive range (up to 460 km) to more broadly map the regional storm evolution than the P-3's TDR. On the other hand, a noted disadvantage of the widely spaced WSR-88Ds is their relatively high average base scan altitude and physical beamwidth at range in comparison to the close-range, fine-scale P-3 TDR measurements. The NEXRAD level II base scan (0.5°) radar reflectivity factors (Crum et al. 1993; Radar Operations Center 1991) are used to map storm precipitation intensity and place the P-3 flight track in the context of the time-dependent storm locations.

[1] Several follow-on studies will employ dual-TDR observations to characterize the bulk morphological attributes of the various storms whose near-inflow is profiled by the CRL.

Brought to you by NOAA Central Library | Unauthenticated | Downloaded 09/08/23 02:59 PM UTC

TABLE 1. Cases of interest with good-quality CRL data during P-3 flight operations, as revealed by numbers of straight flight legs from 2018 (VSE18) and 2019 P-3 (TORUS-2019).

VORTEX-SE (2018)				TORUS (2019)			
Case	Location	Time	Legs	Case	Location	Time	Legs
1	MS	2216–2250 UTC 10 Mar	8	1	CO to NE	2142–2331 UTC 27 May	13
2	MS	2300–2337 UTC 10 Mar	7	2	CO to NE	2346 UTC 27 May–0132 UTC 28 May	13
3	MS	2352 UTC 10 Mar–0110 UTC 11 Mar	12	3	KS	2005–2216 UTC 8 Jun	17
4	AL	2257–2355 UTC 19 Mar	8	4	KS	2311 UTC 8 Jun–0053 UTC 9 Jun	12
5	AL	2357 UTC 19 Mar–0021 UTC 20 Mar	5	5	KS	0054–0153 UTC 9 Jun	7
6	AR	2216–2324 UTC 3 Apr	10	6	OK	2317–2340 UTC 11 Jun	4
7	LA	2035–2108 UTC 13 Apr	5	7	TX	2314 UTC 15 Jun–0033 UTC 16 Jun	7
8	LA	2109–2153 UTC 13 Apr	6	8	TX	2058–2247 UTC 16 Jun	14
9	AR	2158–2234 UTC 13 Apr	8	9	TX	2255–2330 UTC 16 Jun	5
10	LA	2314 UTC 13 Apr–0008 UTC 14 Apr	12				
11	LA to AR	0014–0134 UTC 14 Apr	14				

e. Convective storm inflow sampling strategy

The P-3 sampled multiple severe and tornadic storms that developed in several events during the VSE18 and TORUS field campaigns. Observations in the southeast United States during VSE18 were obtained from 10 March to 14 April 2018, while observations on the Great Plains during TORUS were obtained from 16 May to 16 June 2019. The P-3 flew to an initial targeted area based on regional weather observations, the day 1 convective outlook product issued by the Storm Prediction Center (SPC), additional forecasts from the regional NWS Forecast Offices, and operational and research numerical weather forecasts. The initial P-3 target area was also chosen in close collaboration with other VSE18 and TORUS ground-based field deployments, to obtain coordinated measurements. An important ancillary objective of VSE18 and TORUS was to obtain fine-scale multi–Doppler radar observations combining the dual TDRs with observations from one or more ground-based radars. After reaching the target area, the onboard NSSL flight science team identified a convective cell with potential to intensify based on real-time NEXRAD radar observations. The P-3 typically flew straight, reversing, roughly 20–30-km-long (~3–5 min) legs along the direction of storm motion, normally maintaining a 10 km setback range from the storm (assuming no weather obstructions) at leg altitudes in the range of ~0.8–1.4 km. This flight pattern facilitated optimal dual-TDR sampling of the storm's airflow and reflectivity morphology, while simultaneously obtaining (daytime) CRL profiles extending down to the surface combined with in situ flight-level wind and state variable measurements.

Table 1 summarizes convective inflow information on locations, sampled periods, and legs conducted in the Southeast during the VSE18 campaign and in the Great Plains during the TORUS campaign. The CRL collected 2D inflow WVMR structures of 11 and 9 convective storms in the VSE18 and TORUS campaigns, respectively. Although the P-3 normally flew near cloud-base heights in clear air, the near-storm flight could be prevented by strong turbulence, unexpected popup storms ahead of flight track, or a storm merging process toward P-3. Cases in Table 1 sampled inflow at adequately close range to the storms (~10 km) with more than four flight legs and with little or no influence from liquid clouds to Raman lidar signals. The storm inflow samples are between 1900 and 0100 UTC, and range from 18 min to over 1 h in duration. The number of sampled legs of a storm inflow range from 4 to 17 to evaluate the temporal evolutions of convective storm inflows.

An illustrative series of P-3 flight tracks of VSE18 in the near-inflow of a decaying supercell storm in Arkansas on 13 April 2018 (case 9 from VSE18 in Table 1), including flight-level WVMR and 2D WVMR vertical profiles below the aircraft, is shown in Fig. 2. The top sides of the inserted WVMR transects in each panel are at nearly ~1 km AGL, while the P-3 flight level is at about 0.95 km AGL. The radar-indicated storm moved northeastward as the aircraft flew reverse tracks following the storm motion at a ~10 km storm-setback distance and sampled the near-storm inflow (Figs. 2a–f). After tracking northeast beginning around 2157 UTC (all times are universal time unless specifically noted) through the storm inflow (Fig. 2a), the P-3 reversed track to the southwest and sampled the storm inflow again (Fig. 2b). The P-3 subsequently repeated the reverse-track leg maneuvers to continue sampling the inflow as the storm moved toward the northeast through 2230 UTC 13 April (Figs. 2c–f; some legs not shown due to NEXRAD radar's ~6-min volume scan interval). The vertical distribution of WVMR, rather than being vertically well-mixed, reveals a complicated profile varying with height in the inflow (Fig. 2). The storm-relative flight-level horizontal wind barbs show ~15–25 kt (1 kt ≈ 0.51 m s^{-1})

Brought to you by NOAA Central Library | Unauthenticated | Downloaded 09/08/23 02:59 PM UTC

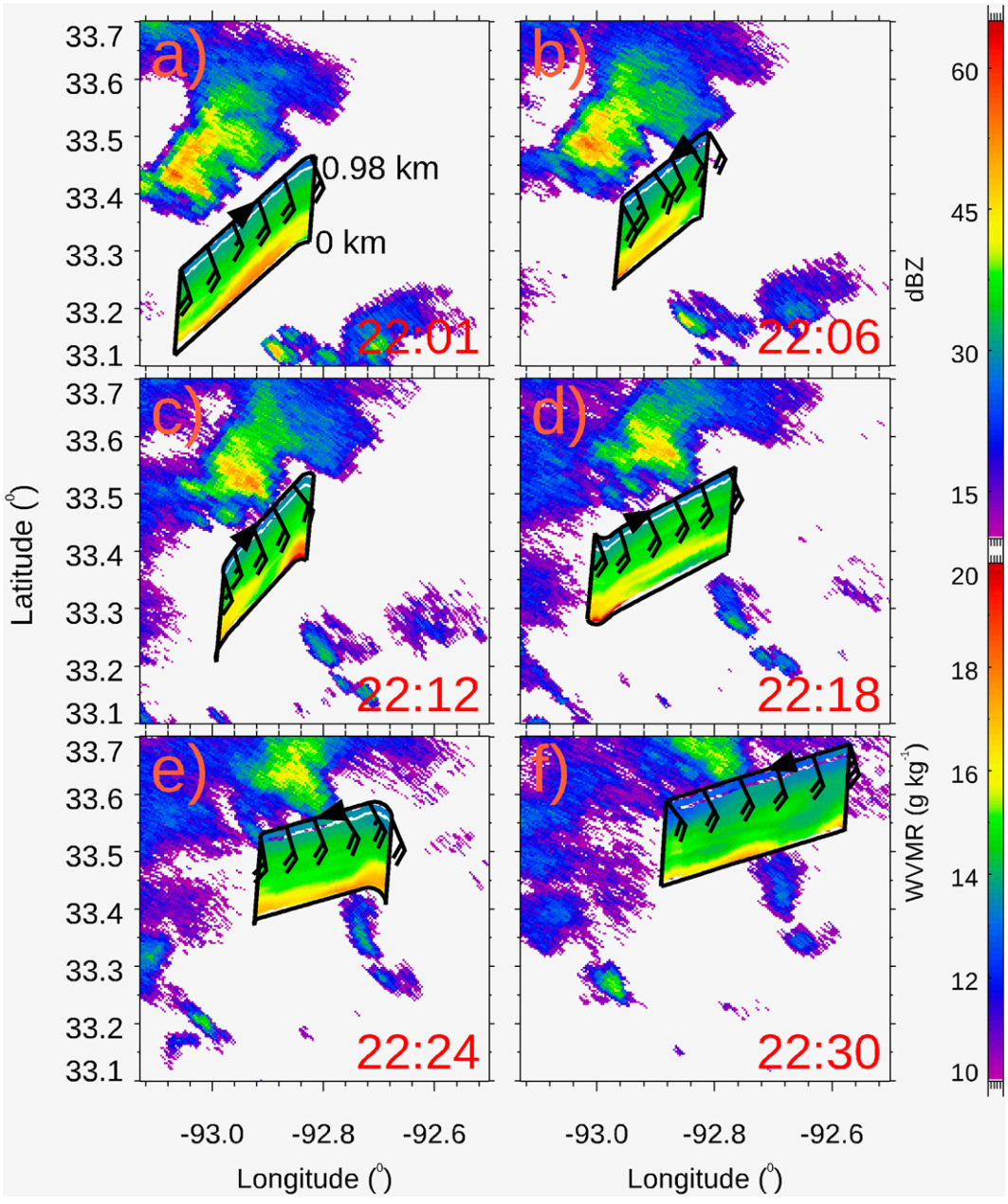

FIG. 2. NEXRAD level II base scan (0.5°) radar reflectivity maps with a vertical WVMR profile along the P-3 flight track at (a) 2201, (b) 2206, (c) 2212, (d) 2218, (e) 2224, and (f) 2230 UTC 13 Apr 2018. The color-coded curves above the CRL 2D profiles are flight level P-3 WVMR values. The wind barbs indicate storm-relative flight-level horizontal winds (full barb equals 10 kt; 1 kt ≈ 0.51 m s^{-1}). The black arrows on the top of transects indicate the flight direction.

southeasterly inflow toward the storm. Since the storm's near-inflow was likely characteristic of its regional warm-sector (i.e., containing no fronts or storm-scale boundaries), the southeasterly flight-level winds imply that some bulk horizontally transported CRL-profiled WVMR subsequently entered the storm's radar echo from the near-inflow BL. The 30 km WVMR transects show the inflow moisture pattern varying with time and distance. The near-surface (<300 m AGL) WVMR varies from 14 to 20 g kg^{-1} within 30 min (Fig. 2) and in a single leg (Fig. 2c). The upper extent (300–1000 m AGL) of WVMR field ranges from about 13 to 14 g kg^{-1} and displays less variability than the near-surface WVMR field.

Another illustrative series of P-3 flight tracks from TORUS with flight-level WVMR and 2D WVMR vertical profiles below the aircraft in the near-inflow of a supercell storm in Texas on 16 June 2019 is shown in Fig. 3 (case 9 from TORUS in Table 1). Case 9 is a nonsevere, isolated storm. The isolated supercell weakens from 2242 to 2326 UTC. The P-3 flew

Brought to you by NOAA Central Library | Unauthenticated | Downloaded 09/08/23 02:59 PM UTC

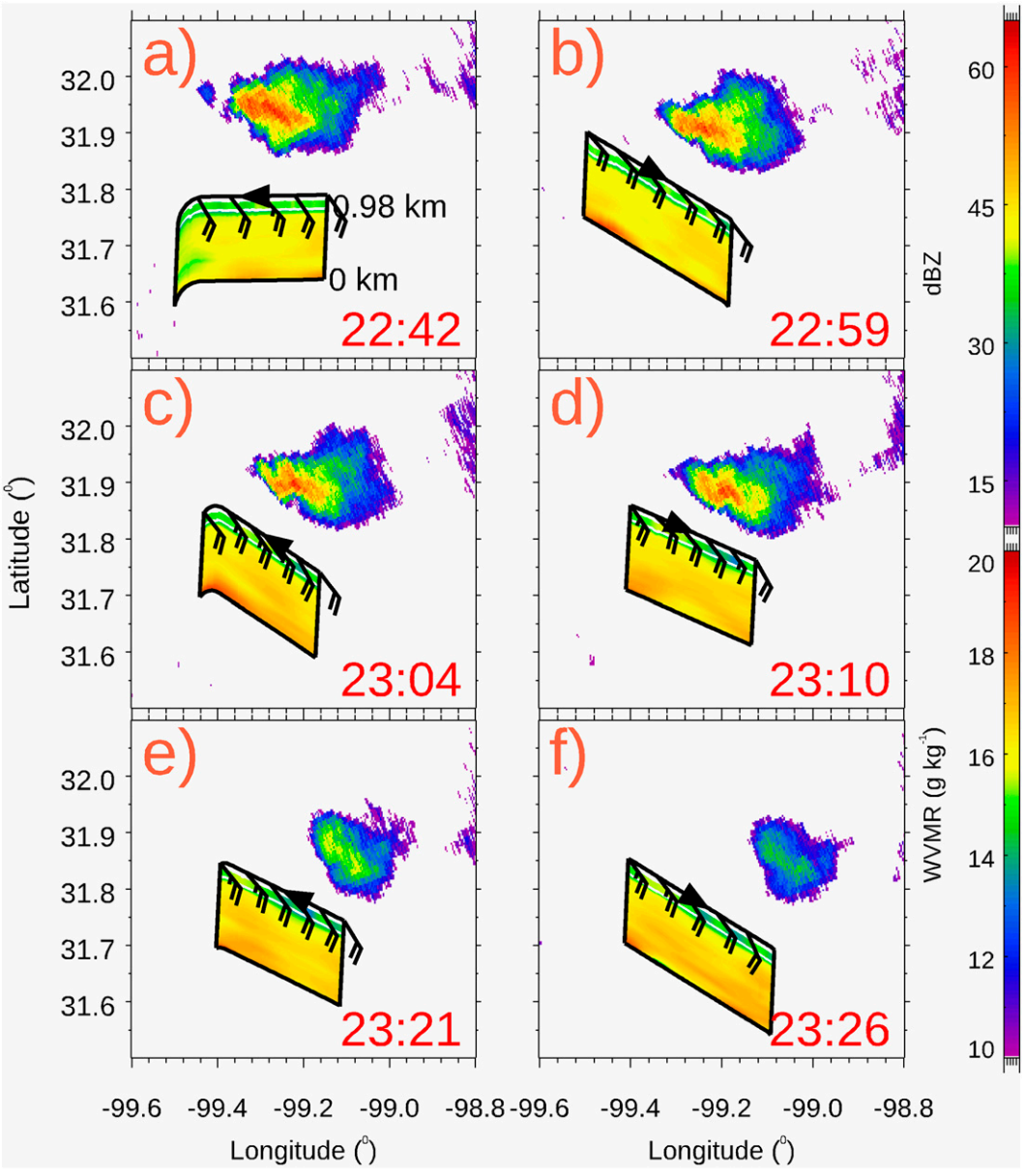

FIG. 3. As in Fig. 2, but at (a) 2242, (b) 2259, (c) 2304, (d) 2310, (e) 2321, and (f) 2326 UTC 16 Jun 2019 (case 9 of TORUS in Table 1).

repeated the reverse-track leg maneuvers to sample the inflow as the storm moved toward the east (Figs. 3c–f; some legs not shown due to NEXRAD radar's ~6-min volume scan interval). The flight-level southeasterly winds have magnitudes of 20–25 kt (Fig. 3). The maximum flight-level storm-relative wind is less than that on 13 April 2018 (Fig. 2). The horizontal WVMR in the low levels show larger WVMR variation from 15 to 17 g kg^{-1} (Fig. 3a) and from 16 to 19 g kg^{-1} (Fig. 3f). These WVMR transects show the inflow moisture pattern varying with time and distance. However, the WVMR is vertically well-mixed from surface to just below the flight level. The vertical WVMR variation in TORUS is less than that in VSE18. The WVMR decreases to 14 g kg^{-1} near the top of the CRL transect (Fig. 3). These WVMR patterns will be discussed in greater detail in section 3.

3. Inflow WVMR structures observed during VSE18 and TORUS

a. Convective storm inflow water vapor structure

The inflow WVMR has different structures in the Southeast and Great Plains regions. The VSE18 project was conducted during March–April 2018, while TORUS was conducted in the Great Plains during May–June 2019. Examples of successive storm-inflow, reverse-track WVMR transects with flight-level in situ WVMR between VSE18 and TORUS are compared

Brought to you by NOAA Central Library | Unauthenticated | Downloaded 09/08/23 02:59 PM UTC

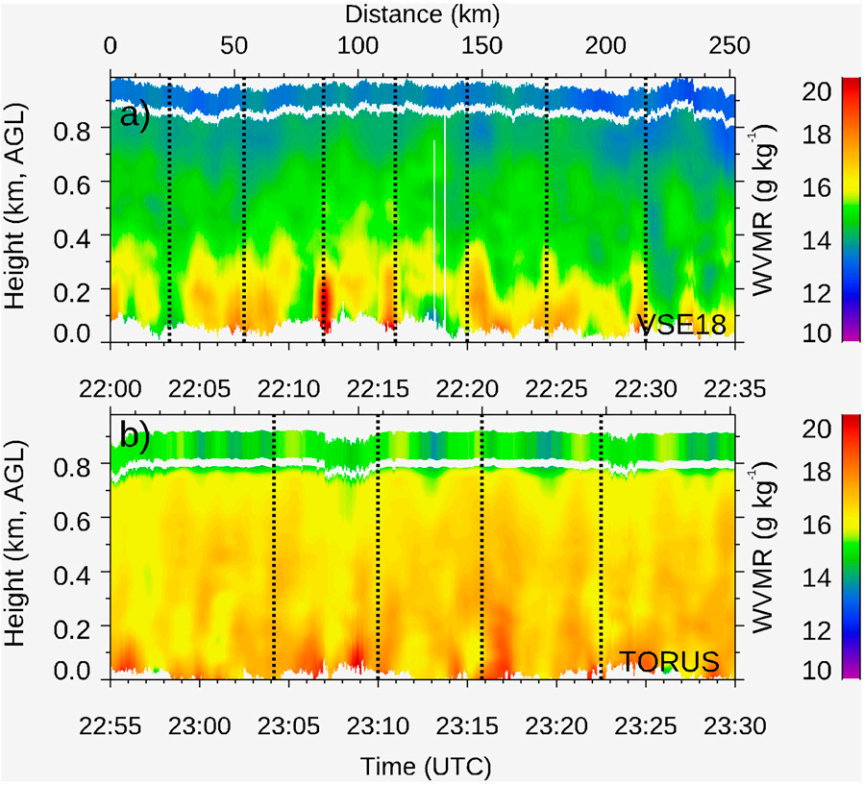

FIG. 4. A 35-min (~250 km) CRL WVMR cross section in the storm inflow region (a) on Apr 13 in the VSE18 (same flight track shown in Fig. 2) and (b) on 16 Jun in the TORUS. The dotted vertical lines are the times of aircraft track reversal.

(Fig. 4). To show the difference in storm inflow between the Southeast and Great Plains region, the clock times of the two examples are almost the same (before sunset) to reduce impacts of PBL evolution at different stages. The sunset time of the VSE18 example is around 0037 UTC (Fig. 4a), while the sunset time of the TORUS example is around 0135 UTC (Fig. 4b). In the Southeast region, the CRL-sampled WVMR below the P-3 flight altitude along the individual storm-following flight legs (with storm-relative locations in Fig. 2) shows pockets with relatively high WVMR values (>16 g kg^{-1}) in the lowest 300 m. The pockets with high WVMR extended lower from 400 to 200 m with time the storm become weak (the radar reflectivity factor decrease from 60 to 40 dBZ; Fig. 2). The WVMR sharply decreases with the height from 14–20 to 13–14 g kg^{-1} from just above the surface to just below flight level (Fig. 4a). The horizontal WVMR profiles become more homogeneous with height with 13–14 g kg^{-1} at height of 800–850 m (Fig. 4a), which is hypothesized to be a result of the decreasing impact of surface-layer vertical latent heat flux with height through the convective boundary layer (CBL). In contrast to the Southeast case, the WVMR in the Great Plains case sustains relatively high values of around 16–18 g kg^{-1} from just above the surface to the height of 0.6 km and is rather homogeneous through the inflow CBL. The WVMR decreases its value from 16 to 14 g kg^{-1} from the upper extent of the CRL transect to the flight level (Fig. 4b). Although only one broadly illustrative case from each region is shown, two examples represent most cases in each region.

To examine PBL stability for the two examples, WVMR, virtual potential temperature (θ_v), and wind barbs at 2231 UTC 13 April 2018 (in the Southeast) and 2311 UTC 16 June 2019 (in the Great Plains) from proximity radiosondes are shown in Fig. 5. These radiosondes are at the far environment (~80 km) compared to the airborne measurements at a distance of 10 km. The WVMR in VSE18 decreases from 14.8 to 13.1 g kg^{-1} from the surface to 1.0 km (Fig. 5a). The WVMR in TORUS decreases from 12 to 10 g kg^{-1} from the surface to 1.0 km (Fig. 5b). The inflow PBL is relatively unstable in the lowest 150 m above the surface (θ_v decreasing with height), and then becomes well-mixed layer from 150 to 400 m (θ_v maintaining its value with height), and becomes stable from 400 to 1000 m (θ_v increasing with height) in the VSE18 case (Fig. 5a). However, the θ_v in TORUS first decreases and then remains steady with height indicating that the PBL has an unstable low level up to 300 m and well-mixed up to 1.2 km (Fig. 5b). These two θ_v structures impact the vertical WVMR distribution. The θ_v profile in VSE18 explains the existence of pockets with relatively high WVMR values (>16 g kg^{-1}) in the lowest 200 m in the WVMR transect (Fig. 4a). The higher θ_v stratification in VSE18 is consistent with the larger PBL veering wind in VSE18: the presence of warm air advection as the easterly

Brought to you by NOAA Central Library | Unauthenticated | Downloaded 09/08/23 02:59 PM UTC

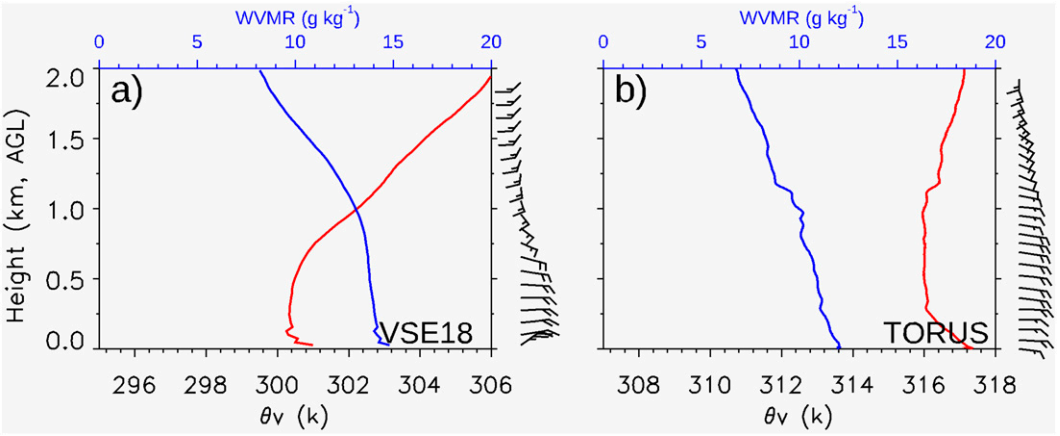

FIG. 5. The radiosonde profiles of WVMR (blue), virtual potential temperature θ_v (red), and storm-relative wind barbs (full barb equals 10 kt) (a) at 2231 UTC 13 Apr 2018 in VSE18 and (b) at 2311 UTC 16 Jun 2019 in TORUS.

wind veers to southeasterly with wind speed decreasing from 25 to 15 kt from surface to 1.0 km, possibly supported by low-level jet features (Fig. 5a). The large low-level horizontal variation of WVMR and large WVMR lapse rates from lower to upper CBL levels in VSE18 are consistent with the hypothesis that the combination of surface-layer latent heat flux and strong vertical wind shear dominates CBL vertical water vapor transport in the SE region. The surface heat processes with complex terrain and land surface types may create inhomogeneous inflow with pockets of very high WVMR in the lower levels, although there is also some indication that higher WVMR values may be preferably located upstream. Neither the P-3 in situ measurements nor widely scattered surface measurements alone are capable of adequately characterizing the regionally averaged WVMR inflow profiles in the SE. However, the wind in TORUS is easterly from surface to 1 km height with a magnitude of 15–20 kt. The inflow moisture in the Great Plains suggests the dominance of a well-mixed inflow with small horizontal variability extending from the surface up to the P-3 flight level.

b. *Systematic inflow water vapor structure*

To explore the systematic vertical WVMR distribution in the two regions, vertical profiles of mean WVMR for every straight flight leg are calculated for the VSE18 and TORUS campaigns. The systematic vertical WVMR distribution refers to the vertical distribution of WVMR of all sampled legs together. Every vertical point represents a 50 m vertical average through a straight flight leg in each of the two mean WVMR profiles. The normalized vertical mean WVMR profiles are obtained by dividing each level by the largest mean WVMR value in the profile. The total number of legs contributing to the averaged VSE18 and TORUS profiles are 95 and 80, respectively. Then, all vertical WVMR profiles are quantified as contour frequency by altitude diagrams (CFADs) over a height range of 0–0.7 km in the VSE18 and TORUS data. The CFAD values are displayed as percentages to distinguish them from normalized WVMR. The CFAD for VSE18 shows the largest percentage of high WVMR (i.e., = 100%) in the lowest level with relatively much lower percentages existing in the middle and upper extent of the CFAD. The mean values of the normalized mean WVMR at every level decrease from 0.99 to 0.84 with height (the black dotted line in Fig. 6a). The normalized WVMR is similarly distributed above 0.5 km with the maximum percentages decreasing less with height. The normalized WVMR in VSE18 again suggests a significant near-surface local vertical transport process of WVMR in the SE region (Fig. 6a). In contrast, the peak of CFAD percentage of the normalized WVMR at each level from TORUS extends from 0.1 to 0.6 km, where the mean values of the normalized mean WVMR at every level show value of 0.92 from the height of 0.0–0.5 km (the black dotted line in Fig. 6b). The vertical CFADs of normalized WVMR in TORUS suggest vertically homogeneous moisture structures in convective storm inflow in the Great Plains (Fig. 5b). The VSE18 normalized WVMR is concentrated between 0.92 and 1 near the surface with the peak CFAD percentages decreasing to 0.85–0.9 with height (Fig. 5a), whereas the peak normalized WVMR is concentrated around 1 extending from 0.1 to 0.6 km in TORUS (Fig. 5b).

The systematic WVMR structures in the Southeast and Great Plains regions reveal the same characteristics of the WVMR structure shown in Fig. 4, respectively. The systematic WVMR with the maximum in the lowest level and decreasing with height in the Southeast region indicates that the surface processes and stable PBL control water vapor variability significantly near the surface. The upper extent of the Southeast CFAD has a relatively uniform distribution, indicating that the impact of surface-layer processes quickly diminishes at about 150 m AGL. The patch-scale local surface latent heat flux accompanying different land surface types and the stable PBL condition creates near-ground inhomogeneity. The horizontal and vertical WVMR gradients, large vertical wind shear, and strong horizontal wind could help force local eddies to mix moisture upward into the storm following the inflow motion (Figs. 4a and 5a). This local latent heating process and stable PBL condition generate the systematic vertical water vapor distribution with the highest water vapor contents mainly located near the surface and decreasing with height in Southeast. The

Brought to you by NOAA Central Library | Unauthenticated | Downloaded 09/08/23 02:59 PM UTC

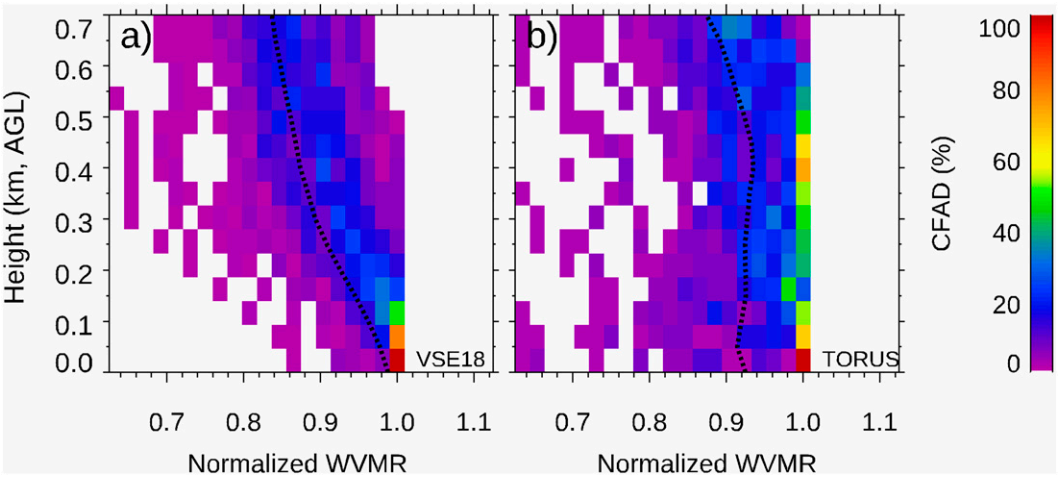

FIG. 6. Contour frequency by altitude diagrams of normalized WVMR of all inflow legs during (a) VSE18 and (b) TORUS campaigns. The black dotted lines represent the height-dependent mean WVMR value. The profile is normalized by the highest value on this profile. The number of legs is 95 in VSE18 and 80 in TORUS.

systematic normalized WVMR, with the maximum probability at each level extending from near the surface to 0.6 km, has the same characteristics as the WVMR structure of TORUS shown in Fig. 4b. The unstable and well-mixed PBL structure (θ_v) facilitates upward eddies mixing of WVMR, even though the wind shear is weak (Fig. 5b) The deep moist inflow is likely well-mixed moist southerly flow in the Great Plains (Fig. 3). The stratified boundary layer could be destabilized by low-level storm outflow being lifted to provide added support for storm evolution (Lin et al. 2019). Therefore, surface heterogeneity and local dynamical processes may dominate the inflow water vapor amount and variability in the Southeast, while the deeply well-mixed moist air controls inflow moisture in the Great Plains.

c. *Comparison of VSE-18 and TORUS near-surface vertical WVMR gradients*

The systematic vertical structures of inflow water vapor suggest that different vertical profiles of horizontal WVMR gradients characterize the Southeast and Great Plains regions (Fig. 7). The complex land surface types resulting in environmental heterogeneity in the PBL could create significantly varying horizontal moisture and wind shear distributions that in turn affect convergence (Katona et al. 2016). The WVMR gradient between 100 and 200 m AGL show different distributions between VSE18 and TORUS (Fig. 7). The probability distributions of WVMR gradient are normalized to the sum of all its possible results as one. The distribution of WVMR gradient in VSE18 ranges from 1 to 16 g kg^{-1} km^{-1}, whereas the WVMR gradient distribution of TORUS has a narrow range from 1 to 5 g kg^{-1} km^{-1} with a maximum frequency around 2 g kg^{-1} km^{-1}. It is noted that, in addition to contribution from land surface heterogeneity, the CFAD frequencies may also be impacted by sampling times and locations relative to storms. The WVMR gradient in the Great Plains cases has a more monodisperse distribution than the Southeast cases. The contrast of WVMR gradient between the VSE18 and TORUS suggests that stronger surface contributions could exist in near-surface water vapor or by LLJ features in the Southeast than in the Great Plains.

4. Inflow WVMR temporal variation and its impact on instability

a. *Impact of water vapor variability on environment instability*

The temporal evolution of WVMR in the convective inflow directly impacts near-storm environmental instability and influences storm evolution. The convective potential can be evaluated by moist static energy (MSE; Emanuel 1994) and CAPE. The MSE can be represented in the form

$$\mathrm{MSE} = C_{pd}T + L_v\mathrm{WVMR} + gz,$$

where T (K) is temperature, WVMR (g kg^{-1}) is the water vapor mixing ratio, C_{pd} (J kg^{-1} K^{-1}) is the specific heat of dry

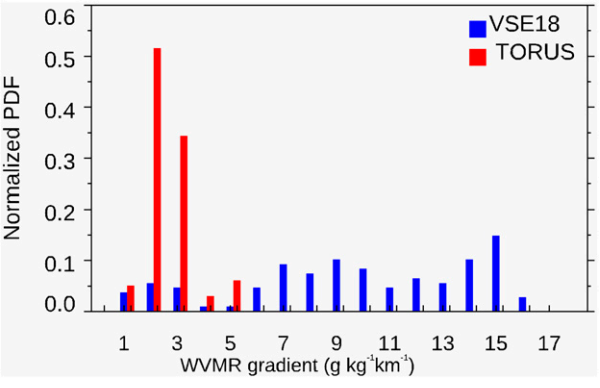

FIG. 7. The normalized probability distributions of vertical WVMR gradient (g kg^{-1} km^{-1}) between the heights of 100 and 200 m AGL of all inflow legs in VSE18 (blue) and TORUS (red). The probability distributions of WVMR gradient are normalized to the sum of all its possible results as one.

Brought to you by NOAA Central Library | Unauthenticated | Downloaded 09/08/23 02:59 PM UTC

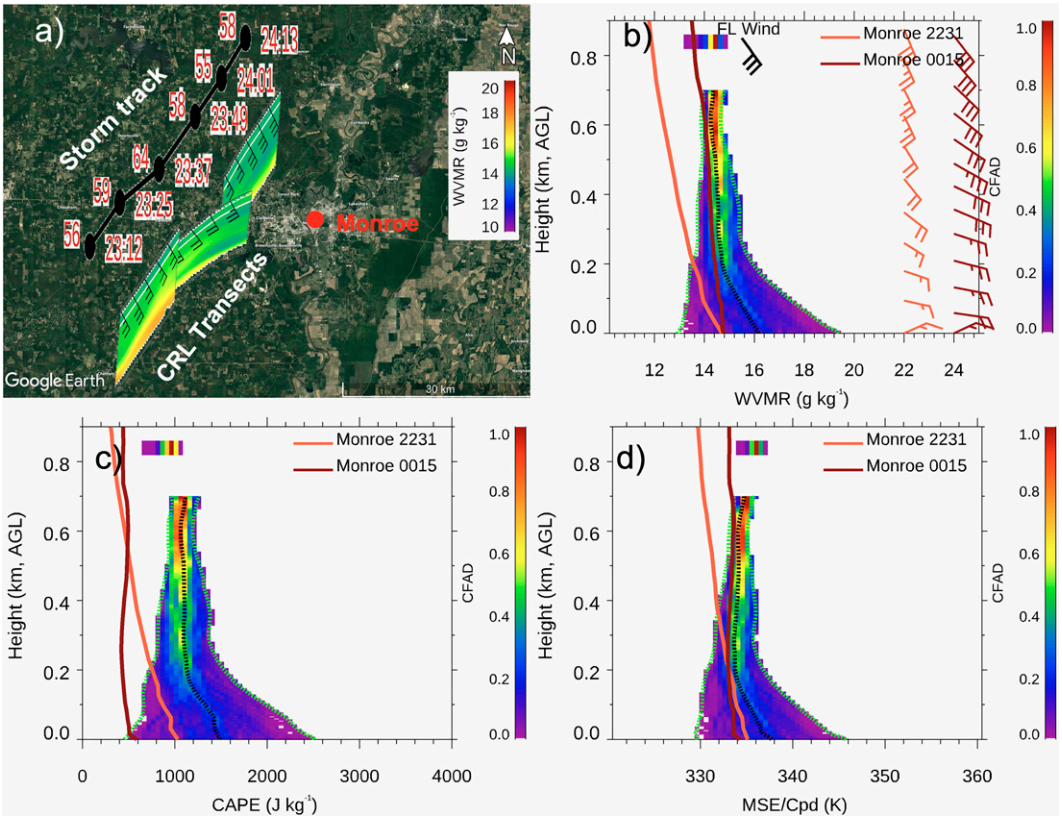

FIG. 8. (a) The storm track showing maximum radar reflectivity factor (dBZ) and time (HH:MM), and three CRL WVMR transects showing flight-level WVMR, flight-level storm-relative wind barbs (full barb equals 10 kt), and radiosonde location (Monroe). (b)–(d) CFADs of (b) WVMR, (c) CAPE, and (d) MSE from CRL data at height from 0.0 to 0.7 km AGL. The plot in (b) depicts flight in situ data at 0.85 km from 2315 to 0008 UTC, along with vertical profiles from two proximity radiosondes at Monroe on 13 Apr 2018. The dashed black lines represent the mean values of WVMR, MSE, and CAPE, while the dashed green lines indicate the mean ± two standard deviations of CRL WVMR, MSE, and CAPE. The wind barbs in (b) are radiosonde wind direction and speed, while the black wind barb is the mean wind at flight level from 2315 to 0008 UTC.

air at constant pressure, L_v (J kg^{-1}) is the latent heat of vaporization, g (m s^{-2}) is gravitational acceleration, and z (m) is the height (MSL). The MSE is approximately conserved under hydrostatic and adiabatic motion, even in the presence of liquid–vapor phase changes (Emanuel 1994). Therefore, MSE can be calculated by combining CRL profiled WVMR with the temperature from neighboring radiosondes. The MSE variation only due to WVMR and height (without temperature) provides a general framework to evaluate the contributions of WVMR variations. The CAPE is a bulk parameter derived by vertically integrating buoyancy from the level of free convection (LFC) to the level of neutral buoyancy (LNB). The instability (CAPE) should be proportional to the integral of the difference between the MSE of a parcel and the environmental saturated MSE through levels where the parcel MSE is larger than the environmental saturated MSE. The WVMR transects of CRL and the temperature profiles from near-launched radiosondes are used to calculate MSE and CAPE. Several proximity radiosonde profiles were modified by substituting the CRL moisture profiles for the low-level sounding moisture below flight level to calculate CAPE and MSE and to compare the impact of moisture variation on instability (Lin et al. 2019). The radiosonde is located in the storm's far-environmental inflow BL, whereas the P-3 measurements at a setback distance of roughly 10–20 km are in the storm's near-environmental inflow. The separation distance between the radiosonde and the P-3 may thus be responsible for some CAPE analysis errors.

To examine the variability of airborne measurements and the difference between CRL measurement and radiosonde, the WVMR, MSE, and CAPE variability with height are compared among the CRL and flight-level in situ data between 2315 UTC 13 April and 0008 UTC 14 April 2018 (case 10 of TORUS) and nearby launched radiosondes in the Southeast (Fig. 8a). Case 10 is a cyclic tornadic supercell storm. Two radiosondes were launched at Monroe, Louisiana, with a distance 30–40 km away from the moving storm, at 2231 and at 0015 UTC, while the CRL continually sampled the storm inflow from 2315 to 0008 UTC (Fig. 8a). By comparing the CRL with flight-level measurements, the upper extent of CRL results are shown to be consistent with results from aircraft in situ measurements at the flight level (Figs. 8a–d).

Brought to you by NOAA Central Library | Unauthenticated | Downloaded 09/08/23 02:59 PM UTC

The mean WVMR of the CRL has a strong vertical gradient from the surface to 0.2 km and a well-mixed structure above 0.2 km (Fig. 8b). Although the WVMR horizontal variability cannot be inferred from the radiosonde profiles, the 0015 UTC sounding is similar to the mean CRL-derived WVMR profile. Although the radiosondes at Monroe were rather closely spaced in time, the radiosonde sampled a much dryer inflow environment at 2231 UTC (Fig. 8b). The radiosonde WVMR at 0015 UTC has smaller difference (<1 g kg^{-1}) than at 2231 UTC (2 g kg^{-1}) compared to the mean CRL WVMR (the black dotted line in Fig. 8b). The horizontal wind speed in the two inflow wind profiles increased with height from the surface to 0.8 km, while the wind direction backed from southeasterly to southerly from 2231 to 0015 UTC. The mean southeasterly flight-level P-3 wind is consistent with the flight-level radiosonde value at 0015 UTC. The CRL-derived WVMR profiles and flight-level P-3 wind and the radiosonde at 0015 UTC indicate the same low-level thermodynamic characteristics, although the P-3 and radiosonde measure "near-environmental" and approximately "far-environmental" storm inflow, respectively (e.g., Wade et al. 2018). Moreover, the 6 g kg^{-1} variation (13–19 g kg^{-1}) detected by the CRL as the SW–NE oriented P-3 legs shifted to the northeast spanning a 1-h period also cannot be resolved by radiosonde data (Fig. 8a). To consider the variation while avoiding either too-large or too-small values of random errors detected by the CRL, we use two standard deviations around the mean to denote the WVMR variability (the green dotted lines in Figs. 8b–d). The CRL WVMR decreases from 13 to 19.5 g kg^{-1} near the surface to 14–15 g kg^{-1} at 0.7 km (Fig. 8b). While the radiosonde-measured WVMR has one value at 0015 UTC, the WVMR variation from the CRL distribution narrows from 4.5 to 1 g kg^{-1} with height.

To understand the covariability of buoyant instability relative to low-level WVMR, the inflow MSE and CAPE profiles calculated by radiosonde data and the CRL are compared. The spatial separation distance between the radiosonde and the P-3 may introduce uncertainties in the CAPE analysis, especially for instances in which there are substantial differences in near- and far-field temperature profiles that could overwhelm WVMR impacts on CAPE differences (as discussed earlier in Fig. 8). The moist static energy is normalized by C_{pd} (K). The CRL MSE variation decreases from 16 K (330–346 K) near the surface to 2 K (334–336 K) at 0.7 km. The Monroe radiosonde sampled the same mesoscale inflow environment at 0015 UTC, although about 30 km away from the storm track (Fig. 8a). The radiosonde-sampled far environment shows 1–4 K MSE difference from the CRL-derived mean MSE through height. The CRL-derived CAPE variation decreases with height from 2000 J kg^{-1} (500–2500 J kg^{-1}) near the surface to 400 J kg^{-1} (900–1300 J kg^{-1}) at 0.7 km. Although Monroe is located ~30 km southeast of the storm track (Fig. 8a), its radiosonde sampled evolving far-environmental inflow conditions from 2231 to 0015 UTC. These far-environmental profiles cannot represent the near-environmental inflow buoyant instability by more than 1–4 K MSE and 100–600 J kg^{-1} CAPE in comparison to the near-environmental CRL-derived inflow mean MSE and CAPE. The difference can be up to 12 K of MSE and 2000 J kg^{-1} of CAPE considering the dual standard deviation ranges of the CRL's values.

As expected, radiosonde measurements far away from the inflow cannot represent the thermodynamic storm inflow conditions (Figs. 8b–d), with the CRL measurement suggesting larger peak values and larger variability in inflow than radiosondes. The roughly 2-hourly radiosonde measurements at Monroe are about 30 km away from the storm, which conventionally otherwise may be considered close enough to characterize storm inflow. The radiosonde sampled a different inflow environment at 2231 UTC from that at 0015 UTC, which is very similar to the CRL and flight-level wind measurements based on WVMR and wind comparison. Inflow WVMR cross sections with 13–19 g kg^{-1} WVMR variability in an hour are unresolved by radiosonde measurements, leading to over 2000 J kg^{-1} instability difference between the CRL and sounding observations. The large variation of WVMR and instability sampled by the CRL support the need for sampling near-storm inflows using novel measurements to improve understanding of convective storm evolution processes.

b. *Inflow WVMR temporal variation and its impact to CAPE*

To investigate the temporal mean WVMR variation difference between the Great Plains and the Southeast region, the temporal WVMR variations are calculated from time series of the individual (roughly 5-min interval) legs. Every point within each mean vertical WVMR temporal variation profile is vertically smoothed by averaging over 50 m spanning each straight flight leg using the following equation:

$$\Delta\mathrm{WVMR} = \frac{\overline{\mathrm{WVMR}_{(\mathrm{leg}_n,Z)}} - \overline{\mathrm{WVMR}_{(\mathrm{leg}_{n-1},Z)}}}{\overline{\mathrm{Time}_{(\mathrm{leg}_n,Z)}} - \overline{\mathrm{Time}_{(\mathrm{leg}_{n-1},Z)}}} \times 5\ \mathrm{min}.$$

$\overline{\mathrm{WVMR}_{(\mathrm{leg}_n,Z)}}$ is the mean WVMR of leg$_n$ at height of Z, and $\overline{\mathrm{Time}_{(\mathrm{leg}_n,Z)}}$ is the mean time at leg$_n$ at height of Z with unit of minute. ΔWVMR is water vapor difference in 5 min.

Using systematic quantitative metrics to succinctly describe this heterogeneity is inherently difficult. The time between successive flight legs cannot be exactly 5 min. The process of transferring time to 5 min could cause some errors in analysis. Systematic differences of water vapor vertical structures and variations as sampled by the CRL exist in convective storm inflow between the Southeast and the Great Plains (Figs. 4 and 6). The CFAD spread of ΔWVMR with a maximum probability of 0.2 at the height of 0.1 km becomes narrower with height with a maximum probability of ~0.9 at 0.7 km in the Southeast, while the CFAD spread of ΔWVMR with a maximum probability of 0.6 at near surface becomes the maximum probability of 0.9 at 0.7 km with height in the Great Plains (Fig. 9). The CFAD spread of ΔWVMR indicate the WVMR is more homogeneous versus height in the Great Plains (Fig. 9b). The CFAD spread of ΔWVMR ranging two standard deviations (the green dotted line) during VSE18 decreases with height over the range of -2 to 1.8 g kg^{-1} (5 min)$^{-1}$ near the surface to -0.38 to 0.38 g kg^{-1} (5 min)$^{-1}$ at 0.7 km (Fig. 9a). In contrast, the CFAD spread ranging two standard deviations

Brought to you by NOAA Central Library | Unauthenticated | Downloaded 09/08/23 02:59 PM UTC

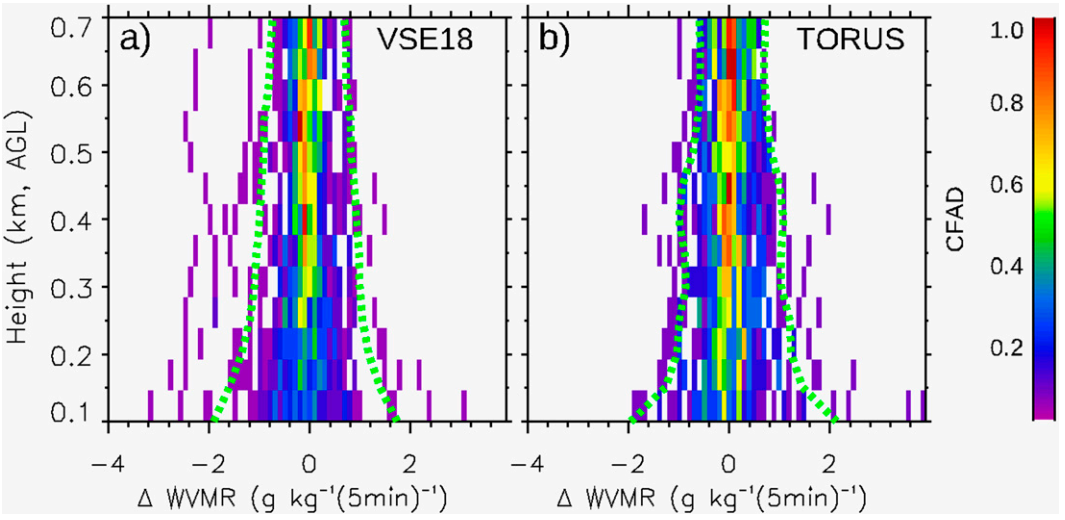

FIG. 9. The CFADs of ΔWVMR in 5 min of all inflow legs during (a) VSE18 and (b) TORUS campaigns. The dashed green lines indicate the mean ± two standard deviations of CRL WVMR variation.

decreases with height over the range of −2 to 2.1 g kg^{-1} (5 min)$^{-1}$ near the surface to −0.28 to 0.28 g kg^{-1} (5 min)$^{-1}$ at 0.7 km in TORUS (Fig. 9b). However, CFAD spreads indicate the maximum magnitude decreases less (from 0.6 to 0.9) with height in TORUS than that (from 0.2 to 0.9) in VSE18.

The CFAD spread of ΔWVMR sharply becomes narrower from a peak probability of 0.2–0.6 from height of 0.1–0.3 km in VSE18, while it is smaller (and relatively homogeneous with height) during TORUS. Based on the contrast of WVMR characteristics and WVMR gradients between VSE18 and TORUS (Figs. 4–7), the near-surface CFADs of WVMR support the hypothesis that stronger surface contributions exist in near-surface water vapor in the Southeast than that in the Great Plains. The moist, deeply well-mixed warm-sector inflow advection appears to dominate ΔWVMR in the surface-based inflow layer below P-3 flight level during TORUS.

The ΔCAPE is calculated the same as the ΔWVMR. The values of ΔCAPE show the significant impact of ΔWVMR on inflow instability (Fig. 10). The rates of CAPE changes are different among different storms. The slope of ΔCAPE indicates the CAPE change per 1 g kg^{-1} WVMR. The slope varies from 336–530 J g^{-1} in VSE18 to 159–564 J g^{-1} during TORUS. The ΔWVMR ranges from −4 to 2.4 g kg^{-1} (5 min)$^{-1}$ and ΔCAPE varies from −1700 to 1300 J kg^{-1} (5 min)$^{-1}$ during VSE18. In contrast, the ΔWVMR ranges from −3.2 to 4 g kg^{-1} (5 min)$^{-1}$ while ΔCAPE varies from −1600 to 1500 J kg^{-1} (5 min)$^{-1}$

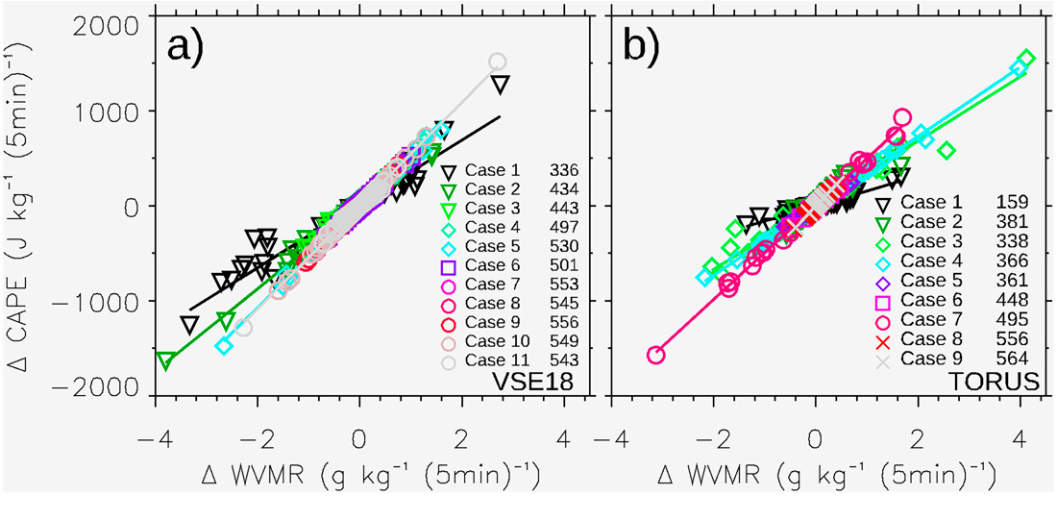

FIG. 10. The relationship between ΔWVMR and ΔCAPE of all inflow legs at heights of 0.1, 0.2, 0.3, 0.4, 0.5, 0.6, and 0.7 km AGL for (a) VSE18 (2018) and (b) TORUS (2019). Cases on the same day use the same symbol. The number on the right for every case represents the slope of the best-fit line.

Brought to you by NOAA Central Library | Unauthenticated | Downloaded 09/08/23 02:59 PM UTC

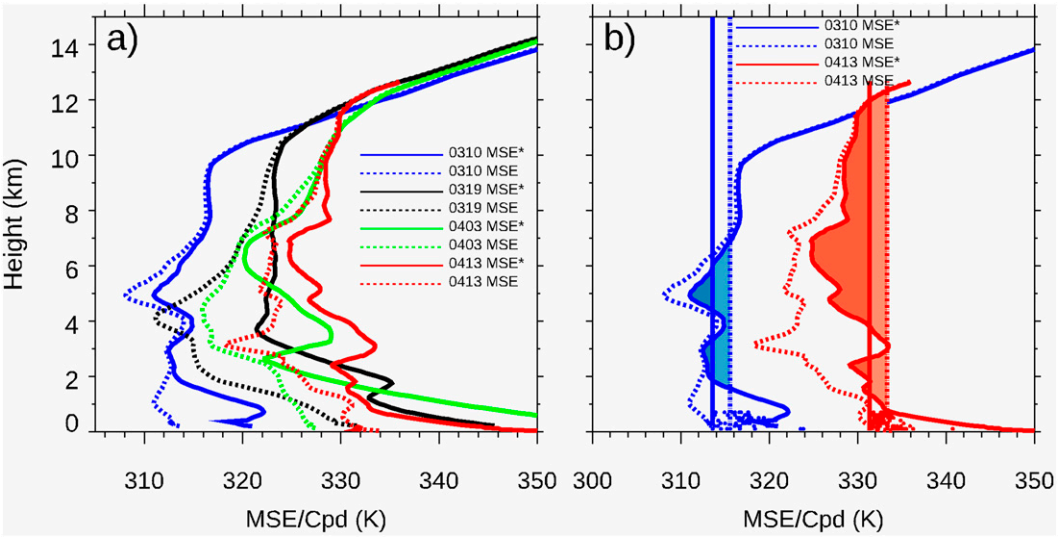

FIG. 11. (a) Radiosondes in aspect of MSE and saturated MSE (MSE*) on 0310, 0319, 0403, and 0413 during VSE18 (case dates are denoted MMDD, where MM is month and DD is day). The solid lines represent MSE* and the dotted lines represent MSE; (b) a comparison of buoyancy between 0310 and 0413. The dots represent CRL-derived PBL MSE near the storms. The vertical solid lines represent the lifting parcel at the surface. The vertical dotted lines represent the lifting parcel increasing 2 K MSE.

during TORUS (Fig. 10). The points with large ΔWVMR exceeding 1.0 g kg^{-1} (5 min)$^{-1}$ are mainly located in lower levels (Fig. 9). The points with ΔWVMR during VSE18 have a broader ΔCAPE than during TORUS (Fig. 10). These different ΔWVMR in low levels could represent contrasting surface-layer flux contributions between the Southeast and the Great Plains based on the contrast of WVMR characteristics and WVMR gradient between the VSE18 and TORUS (Figs. 4–7).

The variations of the slope are dependent on the initial level of CRL data (the lifting level of a parcel) and upper-level radiosonde. The cases on the same day use the same radiosonde measurements to define middle- and upper-tropospheric environmental profiles, which allows CAPE variations to be reliably represented by water vapor changes. The CAPE of cases from different days depends on low-level water vapor changes and also upper-level radiosonde changes. The radiosondes on 0310, 0319, 0403, and 0413 (MMDD; see caption) presenting as MSE (dotted lines) and saturated MSE (solid lines) varying with height are shown in Fig. 11. The upper extent of saturated MSE from radiosondes is rather close over 12 km. Since the actual MSE (dotted lines) is lower than saturated MSE (MSE*; solid line) in the lowest 1 km, the buoyancy in this layer is negative, and the environment does not support storm development (Fig. 11a). However, if the parcel lifted at surface detected by radiosondes, the deep blue area and deep red area on 0310 and 0413 are the integrated buoyancy (CAPE), respectively. The CRL MSE data on 0310 and 0413 could have 2K MSE variation with increasing integrated buoyancy (light blue shaded and light red shaded area). The larger buoyancy (light shaded red) exists on 0413 than on 0310 (Fig. 11b). The increasing areas determined by initial parcel level and MSE* profiles impact the slopes of CAPE and WVMR variation rates in all cases (Fig. 10).

The low-level WVMR variability can cause slope variation. All cases in VSE18 have slope variations of 336–501 J g^{-1} (Fig. 10). For the 10 March case only during VSE18, the upper-layer conditions are the same from case 1 to case 3, but the slope varies from 336 to 434 J g^{-1} indicating 336–434 J kg^{-1} CAPE variation per 1 g kg^{-1} on the 10 March cases where the slope variation is only based on low-level conditions. Moreover, temporal WVMR variations between the successive 5-min interval legs in low levels could lead to higher CAPE variations during VSE18 than during TORUS. Together with Figs. 4 and 10, the CRL observations during VSE18 and TORUS indicate that inflow water vapor environments are significantly different in tornadic environments in the Great Plains and southeast region. The 5-min-interval temporal water vapor variations translate to over 1000 J kg^{-1} CAPE changes in both VSE18 and TORUS, a difference that could significantly modulate storm intensification or decay (Ziegler et al. 2010; Davenport and Parker 2015; Davenport et al. 2019).

5. Summary

This study uses airborne compact Raman lidar (CRL) profiles and in situ flight level measurements obtained by the NOAA P-3 research aircraft to demonstrate the systematic differences between moist inflows and their temporal variability impacting convective potential in the U.S. Great Plains and Southeast regions. The CRL's ability to obtain repeated 2D transects via the P-3 storm-following legs enables the mapping of critically important WVMR morphology and evolution of the storm-inflow boundary layer. The comparison between the CRL and proximity radiosonde measurements indicates that the novel airborne measurements, collected closer to the storms, provide a more complete picture of storm inflow characteristics.

Brought to you by NOAA Central Library | Unauthenticated | Downloaded 09/08/23 02:59 PM UTC

The bulk inflow boundary layer water vapor structures are also different between the Great Plains and the Southeast. The VSE18 results suggest that the surface processes and strong wind shear control water vapor variations to a significant degree in lower levels around storms, which is supported by the general vertical water vapor distribution with the largest magnitude of WVMR mainly located near the surface. Therefore, surface heterogeneity and local dynamical processes could impact the inflow water vapor amount and variation. The normalized water vapor profiles in TORUS show more vertically homogeneous profiles with relatively limited WVMR variability occurring in a deep, moist stratified inflow boundary layer.

The storm inflow WVMR variation rate presents a unique data element obtained by following storm motion in the present study. The WVMR variation rate reveals important details of the inflow evolution. There are also different systematic water vapor variation structures between the Great Plains and the Southeast. The WVMR variation rate has a broader distribution in low levels and becomes more concentrated in the upper extent during VSE18. In contrast, the distribution of WVMR variation rate is relatively homogeneous with height during TORUS. The contrasts of WVMR gradient between VORTEX-SE and TORUS suggest that stronger surface contributions could exist in near-surface water vapor content in the Southeast region than are typically present in the Great Plains.

The CAPE, derived by using proximity radiosondes, identifies the magnitude of environmental instability for the rapidly evolving near-storm BL. Temporal water vapor variations within 5-min periods could lead to changes of over 1000 J kg^{-1} in CAPE in both VSE18 and TORUS, an amount which could significantly impact storm intensification or decay. Moreover, the CAPE changes have a more pronounced impact on low-CAPE convective environments in the Southeast than Great Plains. The rates of CAPE changes are not only different among different storms in the Southeast region and Great Plains according to upper-atmospheric conditions, but also according to the low-level conditions on the same day. These temporal instability evolutions of moving storms are difficult to sample by operational radiosondes, and to a lesser degree also by fixed ground lidars, yet have a potentially large impact on storm evolution. This 1000 J kg^{-1} represents the theoretical upper limit of destabilization that could occur if the storm updraft ingested air entirely comprised of the presented low-level moisture content. In reality, updraft parcels are sourced from a much deeper layer (i.e., the storm's effective inflow layer)—often more than 1250 m deep, based on the supercells analyzed in Thompson et al. (2007). Therefore, although storm updrafts would certainly be impacted regardless by this low-level moisture availability, the extent to which the storm is realistically responding or "tapping into" that destabilization is likely less than that theoretical upper bound.

This observational study illustrates the significant differences in storm-inflow water vapor contents and the importance of spatiotemporal WVMR variation to instability during the severe weather seasons between the U.S. Southeast and Great Plains regions based on the VSE18 and TORUS observations. The airborne measurements of vertical moisture structure and temporal moisture variation in the boundary layer using storm-following airborne measurements provide a unique thermodynamic perspective to study the inflow into fast-moving convective storms. These vertical boundary layer thermodynamic structures help to depict characteristics of the convective storm inflow in the two regions and, were similar observations to be available operationally, would subsequently improve the ability to assess severe weather threats more accurately. It should be noted that the results of the convective storm inflows in both campaigns are too limited in spatial coverage and duration to obtain a robust climatological conclusion. The first step of any future work in this area should be to collect a larger sample of simultaneous thermodynamic inflow conditions near storms. A larger number of inflow samples may also help refine the identification of critical moisture and temperature distributions in storm inflows to better understand the essential thermodynamic inflow structure of storms.

All cases presented herein have severe convection present and in progress. Therefore, inferences cannot be made in regard to the impacts of these differences in WVMR availability on storm initiation. This study covered only a small part of the CAPE–shear parameter space and storm intensity/severity range. The separation distance between the radiosonde and the P-3 may introduce uncertainty in the CAPE analysis. The near-surface attributes (like differing land surface conditions) that differences in Southeast vertical WVMR structure are attributed to presumably exist even without the presence of convection. It is not clear whether the characteristics of the analyzed storms are uniquely tied to these WVMR differences. In a future study, the link between the storm inflow WVMR and the storm intensity will be analyzed. The water vapor in the inflow is but one of the factors impacting storm evolution. There is a time lag between ambient moisture variations and storm response. The onboard dual TDR with dual-Doppler synthesis can reconstruct the flow structures of storms. Together with CRL sampled inflow WVMR structures, lagged correlation between the inflow WVMR and storm intensity will be analyzed. Such analysis will need to take into account other processes that may impact their maintenance and morphology, such as storm-induced alterations to the inflow wind profile, interactions with nearby storms and outflow boundaries, and changes in effective inflow-layer properties in response to evening PBL transition.

Acknowledgments. This study was funded and supported by the National Science Foundation (NSF) Grants AGS-1917693 and AGS-1917701 and by NASA 80NSSC20K0663, with additional support for scientific airborne data collection activities provided to NSSL project staff by the NSSL Director's Discretionary Research Fund. We thank the administrative and engineering staff and flight crews from the National Oceanic and Atmospheric Administration (NOAA) Aircraft Operations Center (AOC) for installing the CRL on WP-3D aircraft NOAA42-RF and acquiring the VORTEX-SE (2018) and TORUS (2019) datasets. A coauthor (CLZ) is acknowledged for his efforts in obtaining NOAA Office of Marine and Aviation Operations (OMAO) flight hour support grants for the P-3 service during both VORTEX-SE and TORUS,

Brought to you by NOAA Central Library | Unauthenticated | Downloaded 09/08/23 02:59 PM UTC

as well as his scientific leadership as P-3 Chief Scientist on these projects. The present study benefitted from the hard work of the many additional VORTEX-SE and TORUS participants to collect the data that helped enable this study. VORTEX-SE and TORUS data are provided by NCAR/EOL (which is funded by NSF) via the respective projects' field catalogs. This manuscript benefits from thoughtful and helpful reviews from three anonymous reviewers.

Data availability statement. The P-3 in situ data and radiosonde data are available from EOL VORTEX-SE 2018 website (https://data.eol.ucar.edu/master_lists/generated/vortex-se_2018) and TORUS website (https://www.eol.ucar.edu/field_projects/torus); the CRL data are available at https://scholar.colorado.edu/concern/datasets/wh246t494.

REFERENCES

Anderson-Frey, A. K., Y. P. Richardson, A. R. Dean, R. L. Thompson, and B. T. Smith, 2019: Characteristics of tornado events and warnings in the southeastern United States. *Wea. Forecasting*, **34**, 1017–1034, https://doi.org/10.1175/WAF-D-18-0211.1.

Ashley, W. S., 2007: Spatial and temporal analysis of tornado fatalities in the United States: 1880–2005. *Wea. Forecasting*, **22**, 1214–1228, https://doi.org/10.1175/2007WAF2007004.1.

——, A. J. Krmenec, and R. Schwantes, 2008: Vulnerability due to nocturnal tornadoes. *Wea. Forecasting*, **23**, 795–807, https://doi.org/10.1175/2008WAF2222132.1.

Bergmaier, P. T., B. Geerts, Z. Wang, B. Liu, and P. C. Campbell, 2014: A dryline in southeast Wyoming. Part II: Airborne in situ and Raman lidar observations. *Mon. Wea. Rev.*, **142**, 2961–2977, https://doi.org/10.1175/MWR-D-13-00314.1.

Brooks, H. E., C. A. Doswell, and M. P. Kay, 2003: Climatological estimates of local daily tornado probability for the United States. *Wea. Forecasting*, **18**, 626–640, https://doi.org/10.1175/1520-0434(2003)018<0626:CEOLDT>2.0.CO;2.

Brown, M. C., C. J. Nowotarski, A. R. Dean, B. T. Smith, R. L. Thompson, and J. M. Peters, 2021: The early evening transition in southeastern U.S. tornado environments. *Wea. Forecasting*, **36**, 1431–1452, https://doi.org/10.1175/WAF-D-20-0191.1.

Buban, M. S., C. L. Ziegler, E. N. Rasmussen, and Y. P. Richardson, 2007: The dryline on 22 May 2002 during IHOP: Ground-radar and in situ data analyses of the dryline and boundary layer evolution. *Mon. Wea. Rev.*, **135**, 2473–2505, https://doi.org/10.1175/MWR3453.1.

Carroll, B. J., B. B. Demoz, D. D. Turner, and R. Delgado, 2021: Lidar observations of a mesoscale moisture transport event impacting convection and comparison to Rapid Refresh model analysis. *Mon. Wea. Rev.*, **149**, 463–477, https://doi.org/10.1175/MWR-D-20-0151.1.

Coniglio, M. C., and M. D. Parker, 2020: Insights into supercells and their environments from three decades of targeted radiosonde observations. *Mon. Wea. Rev.*, **148**, 4893–4915, https://doi.org/10.1175/MWR-D-20-0105.1.

——, J. Correia Jr., P. T. Marsh, and F. Kong, 2013: Verification of convection-allowing WRF Model forecasts of the planetary boundary layer using sounding observations. *Wea. Forecasting*, **28**, 842–862, https://doi.org/10.1175/WAF-D-12-00103.1.

——, G. S. Romine, D. D. Turner, and R. D. Torn, 2019: Impacts of targeted AERI and Doppler lidar wind retrievals on short-term forecasts of the initiation and early evolution of thunderstorms. *Mon. Wea. Rev.*, **147**, 1149–1170, https://doi.org/10.1175/MWR-D-18-0351.1.

Crook, N. A., 1996: Sensitivity of moist convection forced by boundary layer processes to low-level thermodynamic fields. *Mon. Wea. Rev.*, **124**, 1767–1785, https://doi.org/10.1175/1520-0493(1996)124<1767:SOMCFB>2.0.CO;2.

Crum, T. D., R. L. Alberty, and D. W. Burgess, 1993: Recording, archiving, and using WSR-88D data. *Bull. Amer. Meteor. Soc.*, **74**, 645–654, https://doi.org/10.1175/1520-0477(1993)074<0645:RAAUWD>2.0.CO;2.

Davenport, C. E., and M. D. Parker, 2015: Impact of environmental heterogeneity on the dynamics of a dissipating supercell thunderstorm. *Mon. Wea. Rev.*, **143**, 4244–4277, https://doi.org/10.1175/MWR-D-15-0072.1.

——, C. L. Ziegler, and M. I. Biggerstaff, 2019: Creating a more realistic idealized supercell thunderstorm evolution via incorporation of base-state environmental variability. *Mon. Wea. Rev.*, **147**, 4177–4198, https://doi.org/10.1175/MWR-D-18-0447.1.

Davies, J. M., 2004: Estimations of CIN and LFC associated with tornadic and nontornadic supercells. *Wea. Forecasting*, **19**, 714–726, https://doi.org/10.1175/1520-0434(2004)019<0714:EOCALA>2.0.CO;2.

——, and A. Fischer, 2009: Environmental characteristics associated with nighttime tornadoes. *Electron. J. Oper. Meteor.*, **10**, 2009-EJ3, http://nwafiles.nwas.org/ej/pdf/2009-EJ3.pdf.

Degelia, S.K., X. Wang, and D. J. Stensrud, 2019: An evaluation of the impact of assimilating AERI retrievals, kinematic profilers, rawinsondes, and surface observations on a forecast of a nocturnal convection initiation event during the PECAN field campaign. *Mon. Wea. Rev.*, **147**, 2739–2764, https://doi.org/10.1175/MWR-D-18-0423.1.

Dowell, D. C., H. B. Bluestein, and D. P. Jorgensen, 1997: Airborne Doppler radar analysis of supercells during COPS-91. *Mon. Wea. Rev.*, **125**, 365–383, https://doi.org/10.1175/1520-0493(1997)125<0365:ADRAOS>2.0.CO;2.

Emanuel, K. A., 1994: *Atmospheric Convection*. Oxford University Press, 580 pp.

Geerts, B., and Coauthors, 2017: The 2015 Plains Elevated Convection at Night field project. *Bull. Amer. Meteor. Soc.*, **98**, 767–786, https://doi.org/10.1175/BAMS-D-15-00257.1.

Grams, J. S., R. L. Thompson, D. V. Snively, J. A. Prentice, G. M. Hodges, and L. J. Reames, 2012: A climatology and comparison of parameters for significant tornado events in the United States. *Wea. Forecasting*, **27**, 106–123, https://doi.org/10.1175/WAF-D-11-00008.1.

Guyer, J. L., and A. R. Dean, 2010: Tornadoes within weak CAPE environments across the continental United States. *25th Conf. on Severe Local Storms*, Denver, CO, Amer. Meteor. Soc., 1.5, https://ams.confex.com/ams/pdfpapers/175725.pdf.

Hu, X.-M., M. Xue, and R. A. McPherson, 2017: The importance of soil-type contrast in modulating August precipitation distribution near the Edwards Plateau and Balcones Escarpment in Texas. *J. Geophys. Res. Atmos.*, **122**, 10 711–10 728, https://doi.org/10.1002/2017JD027035.

Hu, X. M., M. Xue, and X. Li, 2019: The use of high-resolution sounding data to evaluate and optimize nonlocal PBL schemes for simulating the slightly stable upper convective boundary layer. *Mon. Wea. Rev.*, **147**, 3825–3841, https://doi.org/10.1175/MWR-D-19-0085.1.

Jorgensen, D. P., M. A. LeMone, and S. B. Trier, 1997: Structure and evolution of the 22 February 1993 TOGA COARE squall line: Aircraft observations of precipitation, circulation, and surface energy fluxes. *J. Atmos. Sci.*, **54**, 1961–1985,

Brought to you by NOAA Central Library | Unauthenticated | Downloaded 09/08/23 02:59 PM UTC

https://doi.org/10.1175/1520-0469(1997)054<1961:SAEOTF>2.0.CO;2.

——, C. L. Ziegler, E. N. Rasmussen, A. S. Goldstein, and A. A. Alford, 2017: Improvements to the NOAA P-3 airborne Doppler tail-mounted radar: Supercell observations from VORTEX-Southeast. *38th AMS Conf. on Radar Meteorology*, Chicago, IL, Amer. Meteor. Soc., 6A.2, https://ams.confex.com/ams/38RADAR/webprogram/Paper320666.html.

Kahn, B. H., and Coauthors, 2011: Temperature and water vapor variance scaling in global models: Comparisons to satellite and aircraft data. *J. Atmos. Sci.*, **68**, 2156–2168, https://doi.org/10.1175/2011JAS3737.1.

Kalthoff, N., H. J. Binder, M. Kossmann, R. Vögtlin, U. Corsmeier, F. Fiedler, and H. Schlager, 1998: Temporal evolution and spatial variation of the boundary layer over complex terrain. *Atmos. Environ.*, **32**, 1179–1194, https://doi.org/10.1016/S1352-2310(97)00193-3.

Katona, B., P. Markowski, C. Alexander, and S. Benjamin, 2016: The influence of topography on convective storm environments in the eastern United States as deduced from the HRRR. *Wea. Forecasting*, **31**, 1481–1490, https://doi.org/10.1175/WAF-D-16-0038.1.

Kerr, B. W., and G. L. Darkow, 1996: Storm-relative winds and helicity in the tornadic thunderstorm environment. *Wea. Forecasting*, **11**, 489–505, https://doi.org/10.1175/1520-0434(1996)011<0489:SRWAHI>2.0.CO;2.

King, J. R., M. D. Parker, K. D. Sherburn, and G. M. Lackmann, 2017: Rapid evolution of cool season, low-CAPE severe thunderstorm environments. *Wea. Forecasting*, **32**, 763–779, https://doi.org/10.1175/WAF-D-16-0141.1.

Lehner, M., and M. W. Rotach, 2018: Current challenges in understanding and predicting transport and exchange in the atmosphere over mountainous terrain. *Atmosphere*, **9**, 276, https://doi.org/10.3390/atmos9070276.

Lin, G., B. Geerts, Z. Wang, C. Grasmick, X. Jing, and J. Yang, 2019: Interactions between a nocturnal MCS and the stable boundary layer as observed by an airborne compact Raman lidar during PECAN. *Mon. Wea. Rev.*, **147**, 3169–3189, https://doi.org/10.1175/MWR-D-18-0388.1.

——, C. Grasmick, B. Geerts, Z. Wang, and M. Deng, 2021: Convection initiation and bore formation following the collision of mesoscale boundaries over a developing stable boundary layer: A case study from PECAN. *Mon. Wea. Rev.*, **149**, 2351–2367, https://doi.org/10.1175/MWR-D-20-0282.1.

Liu, B., Z. Wang, Y. Cai, P. Wechsler, W. Kuestner, M. Burkhart, and W. Welch, 2014: Compact airborne Raman lidar for profiling aerosol, water vapor and clouds. *Opt. Express*, **22**, 20 613–20 621, https://doi.org/10.1364/OE.22.020613.

Maddox, R. A., 1976: An evaluation of tornado proximity wind and stability data. *Mon. Wea. Rev.*, **104**, 133–142, https://doi.org/10.1175/1520-0493(1976)104<0133:AEOTPW>2.0.CO;2.

Markowski, P. M., and N. Dotzek, 2011: A numerical study of the effects of orography on supercells. *Atmos. Res.*, **100**, 457–478, https://doi.org/10.1016/j.atmosres.2010.12.027.

——, and Coauthors, 2012: The pretornadic phase of the Goshen County, Wyoming, supercell of 5 June 2009 intercepted by VORTEX2. Part I: Evolution of kinematic and surface thermodynamic fields. *Mon. Wea. Rev.*, **140**, 2887–2915, https://doi.org/10.1175/MWR-D-11-00336.1.

Mueller, D., B. Geerts, Z. Wang, M. Deng, and C. Grasmick, 2017: Evolution and vertical structure of an undular bore observed on 20 June 2015 during PECAN. *Mon. Wea. Rev.*, **145**, 3775–3794, https://doi.org/10.1175/MWR-D-16-0305.1.

Nelson, T. C., L. Harrison, and K. L. Corbosiero, 2020: Temporal and spatial autocorrelations from expendable digital dropsondes (XDDs) in tropical cyclones. *J. Atmos. Oceanic Technol.*, **37**, 381–399, https://doi.org/10.1175/JTECH-D-19-0032.1.

Nielsen, E. R., G. R. Herman, R. C. Tournay, J. M. Peters, and R. S. Schumacher, 2015: Double impact: When both tornadoes and flash floods threaten the same place at the same time. *Wea. Forecasting*, **30**, 1673–1693, https://doi.org/10.1175/WAF-D-15-0084.1.

Peters, J. M., E. R. Nielsen, M. D. Parker, S. M. Hitchcock, and R. S. Schumacher, 2017: The impact of low-level moisture errors on model forecasts of an MCS observed during PECAN. *Mon. Wea. Rev.*, **145**, 3599–3624, https://doi.org/10.1175/MWR-D-16-0296.1.

Potvin, C. K., K. L. Elmore, and S. J. Weiss, 2010: Assessing the impacts of proximity sounding criteria on the climatology of significant tornado environments. *Wea. Forecasting*, **25**, 921–930, https://doi.org/10.1175/2010WAF2222368.1.

Radar Operations Center, 1991: NOAA Next Generation Radar (NEXRAD) level 2 base data. NOAA National Centers for Environmental Information, accessed 4 April 2022, https://doi.org/10.7289/V5W9574V.

Rasmussen, E. N., 2015: VORTEX-Southeast program overview. National Severe Storms Laboratory Rep., 36 pp.

——, and D. O. Blanchard, 1998: A baseline climatology of sounding-derived supercell and tornado forecast parameters. *Wea. Forecasting*, **13**, 1148–1164, https://doi.org/10.1175/1520-0434(1998)013<1148:ABCOSD>2.0.CO;2.

——, J. M. Straka, R. P. Davies-Jones, C. A. Doswell, F. H. Carr, M. D. Eilts, and D. R. MacGorman, 1994: Verification of the Origins of Rotation in Tornadoes Experiment: VORTEX. *Bull. Amer. Meteor. Soc.*, **75**, 995–1006, https://doi.org/10.1175/1520-0477(1994)075<0995:VOTOOR>2.0.CO;2.

Rogers, R., S. Lorsolo, P. Reasor, J. Gamache, and F. Marks, 2012: Multiscale analysis of tropical cyclone kinematic structure from airborne Doppler radar composites. *Mon. Wea. Rev.*, **140**, 77–99, https://doi.org/10.1175/MWR-D-10-05075.1.

Satrio, M. A., D. J. Bodine, A. E. Reinhart, T. Maruyama, and F. T. Lombardo, 2020: Understanding how complex terrain impacts tornado dynamics using a suite of high-resolution numerical simulations. *J. Atmos. Sci.*, **77**, 3277–3300, https://doi.org/10.1175/JAS-D-19-0321.1.

Schneider, R. S., S. J. Weiss, and P. D. Bothwell, 2006: Analysis of estimated environments for 2004 and 2005 severe convective storm reports. *23rd Conf. on Severe Local Storms*, Saint Louis, MO, Amer. Meteor. Soc., 3.5, https://ams.confex.com/ams/23SLS/techprogram/paper_115246.htm.

Schultz, C. J., and M. A. Askelson, 2012: Vertical variations of boundary layer potential buoyancy in tornadic and nontornadic near-storm environments. *Wea. Forecasting*, **27**, 1489–1506, https://doi.org/10.1175/WAF-D-11-00097.1.

Schumacher, R. S., 2015: Sensitivity of precipitation accumulation in elevated convective systems to small changes in low-level moisture. *J. Atmos. Sci.*, **72**, 2507–2524, https://doi.org/10.1175/JAS-D-14-0389.1.

——, and J. M. Peters, 2017: Near-surface thermodynamic sensitivities in simulated extreme-rain-producing mesoscale convective systems. *Mon. Wea. Rev.*, **145**, 2177–2200, https://doi.org/10.1175/MWR-D-16-0255.1.

Sherburn, K. D., and M. D. Parker, 2014: Climatology and ingredients of significant severe convection in high-shear, low-CAPE environments. *Wea. Forecasting*, **29**, 854–877, https://doi.org/10.1175/WAF-D-13-00041.1.

Brought to you by NOAA Central Library | Unauthenticated | Downloaded 09/08/23 02:59 PM UTC

——, ——, J. R. King, and G. M. Lackmann, 2016: Composite environments of severe and nonsevere high-shear, low-CAPE convective events. *Wea. Forecasting*, **31**, 1899–1927, https://doi.org/10.1175/WAF-D-16-0086.1.

Stechman, D. M., G. McFarquhar, R. Rauber, B. Jewett, and R. Black, 2020: Composite in situ microphysical analysis of all spiral vertical profiles executed within BAMEX and PECAN mesoscale convective systems. *J. Atmos. Sci.*, **77**, 2541–2565, https://doi.org/10.1175/JAS-D-19-0317.1.

Steinke, S., S. Eikenberg, U. Löhnert, G. Dick, D. Klocke, P. Di Girolamo, and S. Crewell, 2015: Assessment of small-scale integrated water vapour variability during HOPE. *Atmos. Chem. Phys.*, **15**, 2675–2692, https://doi.org/10.5194/acp-15-2675-2015.

Terti, G., I. Ruin, S. Anquetin, and J. J. Gourley, 2017: A situation-based analysis of flash flood fatalities in the United States. *Bull. Amer. Meteor. Soc.*, **98**, 333–345, https://doi.org/10.1175/BAMS-D-15-00276.1.

Thompson, R. L., R. Edwards, J. A. Hart, K. L. Elmore, and P. Markowski, 2003: Close proximity soundings within supercell environments obtained from the Rapid Update Cycle. *Wea. Forecasting*, **18**, 1243–1261, https://doi.org/10.1175/1520-0434(2003)018<1243:CPSWSE>2.0.CO;2.

——, ——, and C. M. Mead, 2004: An update to the supercell composite and significant tornado parameters. *22nd Conf. on Severe Local Storms*, Hyannis, MA, Amer. Meteor. Soc., P8.1, https://www.spc.noaa.gov/publications/thompson/stp_scp.pdf.

——, C. M. Mead, and R. Edwards, 2007: Effective storm-relative helicity and bulk shear in supercell thunderstorm environments. *Wea. Forecasting*, **22**, 102–115, https://doi.org/10.1175/WAF969.1.

Wade, A. R., M. C. Coniglio, and C. L. Ziegler, 2018: Comparison of near-and far-field supercell inflow environments using radiosonde observations. *Mon. Wea. Rev.*, **146**, 2403–2415, https://doi.org/10.1175/MWR-D-17-0276.1.

Wang, Z., 2020: Airborne compact Raman lidar (CRL) water vapor and temperature profiles, version 2.0. UCAR/NCAR Earth Observing Laboratory, accessed 8 December 2020, https://doi.org/10.26023/JYNH-KCZE-910F.

Weckwerth, T. M., 2000: The effect of small-scale moisture variability on thunderstorm initiation. *Mon. Wea. Rev.*, **128**, 4017–4030, https://doi.org/10.1175/1520-0493(2000)129<4017:TEOSSM>2.0.CO;2.

——, and D. B. Parsons, 2006: A review of convection initiation and motivation for IHOP_2002. *Mon. Wea. Rev.*, **134**, 5–22, https://doi.org/10.1175/MWR3067.1.

——, J. W. Wilson, and R. M. Wakimoto, 1996: Thermodynamic variability within the convective boundary layer due to horizontal convective rolls. *Mon. Wea. Rev.*, **124**, 769–784, https://doi.org/10.1175/1520-0493(1996)124<0769:TVWTCB>2.0.CO;2.

——, and Coauthors, 2004: An overview of the International H_2O Project (IHOP_2002) and some preliminary highlights. *Bull. Amer. Meteor. Soc.*, **85**, 253–278, https://doi.org/10.1175/BAMS-85-2-253.

——, J. Hanesiak, J. W. Wilson, S. B. Trier, S. K. Degelia, W. A. Gallus Jr., R. D. Roberts, and X. Wang, 2019: Nocturnal convection initiation during PECAN 2015. *Bull. Amer. Meteor. Soc.*, **100**, 2223–2239, https://doi.org/10.1175/BAMS-D-18-0299.1.

Weisman, M. L., and Coauthors, 2015: The Mesoscale Predictability Experiment (MPEX). *Bull. Amer. Meteor. Soc.*, **96**, 2127–2149, https://doi.org/10.1175/BAMS-D-13-00281.1.

Wu, D., and Coauthors, 2016: Airborne compact rotational Raman lidar for temperature measurement. *Opt. Express*, **24**, A1210–A1223, https://doi.org/10.1364/OE.24.0A1210.

Wulfmeyer, V., H. S. Bauer, M. Grzeschik, A. Behrendt, F. Vandenberghe, E. V. Browell, S. Ismail, and R. A. Ferrare, 2006: Four-dimensional variational assimilation of water vapor differential absorption lidar data: The first case study within IHOP_2002. *Mon. Wea. Rev.*, **134**, 209–230, https://doi.org/10.1175/MWR3070.1.

Wurman, J., D. Dowell, Y. Richardson, P. Markowski, E. Rasmussen, D. Burgess, L. Wicker, and H. B. Bluestein, 2012: The Second Verification of the Origins of Rotation in Tornadoes Experiment: VORTEX2. *Bull. Amer. Meteor. Soc.*, **93**, 1147–1170, https://doi.org/10.1175/BAMS-D-11-00010.1.

Yang, J., and Coauthors, 2013: The role of satellite remote sensing in climate change studies. *Nat. Climate Change*, **3**, 875–883, https://doi.org/10.1038/nclimate1908.

Ziegler, C. L., 2013: A diabatic Lagrangian technique for the analysis of convective storms. Part II: Application to a radar-observed storm. *J. Atmos. Oceanic Technol.*, **30**, 2266–2280, https://doi.org/10.1175/JTECH-D-13-00036.1.

——, 2019: NOAA P-3 flight level data, version 1.0. UCAR/NCAR Earth Observing Laboratory, accessed 4 April 2022, https://doi.org/10.26023/KE00-Q146-290Y.

——, and C. E. Hane, 1993: An observational study of the dryline. *Mon. Wea. Rev.*, **121**, 1134–1151, https://doi.org/10.1175/1520-0493(1993)121<1134:AOSOTD>2.0.CO;2.

——, and E. N. Rasmussen, 1998: The initiation of moist convection at the dryline: Forecasting issues from a case study perspective. *Wea. Forecasting*, **13**, 1106–1131, https://doi.org/10.1175/1520-0434(1998)013<1106:TIOMCA>2.0.CO;2.

——, ——, T. R. Shepherd, A. I. Watson, and J. M. Straka, 2001: The evolution of low-level rotation in the 29 May 1994 Newcastle–Graham, Texas, storm complex during VORTEX. *Mon. Wea. Rev.*, **129**, 1339–1368, https://doi.org/10.1175/1520-0493(2001)129<1339:TEOLLR>2.0.CO;2.

——, ——, M. S. Buban, Y. P. Richardson, L. J. Miller, and R. Rabin, 2007: The "triple point" on 24 May 2002 during IHOP. Part II: Ground-radar and in situ boundary layer analysis of cumulus development and convection initiation. *Mon. Wea. Rev.*, **135**, 2443–2472, https://doi.org/10.1175/MWR3411.1.

——, E. R. Mansell, J. M. Straka, D. R. MacGorman, and D. W. Burgess, 2010: The impact of spatial variations of low-level stability on the life cycle of a simulated supercell storm. *Mon. Wea. Rev.*, **138**, 1738–1766, https://doi.org/10.1175/2009MWR3010.1.

——, T. Murphy, K. Elmore, M. I. Biggerstaff, Z. Wang, E. N. Rasmussen, D. P. Jorgensen, and A. A. Alford, 2018: Kinematics, thermodynamics, and microphysics of the tornadic 13-14 April 2018 Calhoun, La supercell during VORTEX-SE. *29th Conf. on Severe Local Storms*, Stowe, VT, Amer. Meteor. Soc., 8.4, https://ams.confex.com/ams/29SLS/webprogram/Paper348224.html.

Brought to you by NOAA Central Library | Unauthenticated | Downloaded 09/08/23 02:59 PM UTC